remote sensing

MDPI

Article

A Machine Learning Algorithm for Himawari-8 Total Suspended Solids Retrievals in the Great Barrier Reef

Larissa Patricio-Valerio [1,2,*], Thomas Schroeder [2], Michelle J. Devlin [3], Yi Qin [4] and Scott Smithers [1]

[1] College of Science and Engineering, James Cook University, Townsville, QLD 4811, Australia; scott.smithers@jcu.edu.au
[2] Commonwealth Scientific and Industrial Research Organisation, Oceans and Atmosphere, GPO Box 2583, Brisbane, QLD 4001, Australia; thomas.schroeder@csiro.au
[3] Centre for Environment Fisheries and Aquaculture Science, Parkfield Road, Lowestoft, Suffolk NR33 0HT, UK; michelle.devlin@cefas.co.uk
[4] Commonwealth Scientific and Industrial Research Organisation, Oceans and Atmosphere, GPO Box 1700, Canberra, ACT 2601, Australia; yi.qin@csiro.au
* Correspondence: larissa.patriciovalerio@my.jcu.edu.au

Abstract: Remote sensing of ocean colour has been fundamental to the synoptic-scale monitoring of marine water quality in the Great Barrier Reef (GBR). However, ocean colour sensors onboard low orbit satellites, such as the Sentinel-3 constellation, have insufficient revisit capability to fully resolve diurnal variability in highly dynamic coastal environments. To overcome this limitation, this work presents a physics-based coastal ocean colour algorithm for the Advanced Himawari Imager onboard the Himawari-8 geostationary satellite. Despite being designed for meteorological applications, Himawari-8 offers the opportunity to estimate ocean colour features every 10 min, in four broad visible and near-infrared spectral bands, and at 1 km^2 spatial resolution. Coupled ocean–atmosphere radiative transfer simulations of the Himawari-8 bands were carried out for a realistic range of in-water and atmospheric optical properties of the GBR and for a wide range of solar and observation geometries. The simulated data were used to develop an inverse model based on artificial neural network techniques to estimate total suspended solids (TSS) concentrations directly from the Himawari-8 top-of-atmosphere spectral reflectance observations. The algorithm was validated with concurrent in situ data across the coastal GBR and its detection limits were assessed. TSS retrievals presented relative errors up to 75% and absolute errors of 2 mg L^{-1} within the validation range of 0.14 to 24 mg L^{-1}, with a detection limit of 0.25 mg L^{-1}. We discuss potential applications of Himawari-8 diurnal TSS products for improved monitoring and management of water quality in the GBR.

Keywords: Himawari-8; ocean colour; artificial neural networks; Great Barrier Reef; coastal waters; total suspended solids; machine learning; water quality

Citation: Patricio-Valerio, L.; Schroeder, T.; Devlin, M.J.; Qin, Y.; Smithers, S. A Machine Learning Algorithm for Himawari-8 Total Suspended Solids Retrievals in the Great Barrier Reef. *Remote Sens.* **2022**, *14*, 3503. https://doi.org/10.3390/rs14143503

Academic Editor: Chris Roelfsema

Received: 15 May 2022
Accepted: 19 July 2022
Published: 21 July 2022

1. Introduction

Ocean colour sensors onboard low Earth orbit (LEO) satellites, such as MODIS/Aqua, VIIRS/Suomi-NPP, and OLCI/Sentinel-3, have provided long-term records of valuable and cost-effective observations to examine daily to inter-annual dynamics of water quality in the Great Barrier Reef (GBR) [1–5]. The LEO satellites scan the same geographic area within one or two days at best; however, the time-lag between two consecutive and identical orbits (i.e., revisit periodicity) commonly varies between one and up to four weeks. In addition, the ocean colour imagery may be largely affected by the presence of clouds and sun glint, limiting the retrieval of high quality observations [6]. This can require a weekly-to-monthly set of daily images from the same area to develop a composite cloudless view of the ocean. Consequently, the temporal capability of LEO satellites is insufficient to develop a comprehensive observational system and to effectively monitor short-term dynamic coastal processes, such as phytoplankton diel cycles, daily progression of flood plumes, and

tidal and wind-driven resuspension [7–9]. Researchers and environmental managers still rely on LEO ocean colour products for acquiring cost-effective spatial information in the coastal GBR [10,11], but recognise the limitations of these techniques to resolve short-term variability.

Satellites on a geostationary Earth orbit (GEO), otherwise, allow near continuous observation of large areas of the globe at higher frequency (minutes to hours) compared to the near daily revisit frequency of LEO platforms, particularly over the tropics [9]. The world's first Geostationary Ocean Colour Imager (GOCI-I), launched in 2010, has revealed the temporal dynamics of rapidly changing coastal processes in Northeast Asia, such as of turbidity plumes and harmful algal blooms [12,13]. Its success provided a useful case for the future development of global GEO ocean colour missions [14]; however, none of the missions proposed for launching within the next decade were designed for observing Australian waters. Nevertheless, GEO satellites are globally operated for meteorological observations and recent technological advances have leveraged their capabilities for collecting data over the oceans, allowing more dynamic processes to be observed from space [15–17]. The next-generation GEO meteorological sensors are equipped with an increased number of bands in the visible spectrum (2 or 3 instead of only 1 band) combined with improved radiometric sensitivity (signal-to-noise ratio) and onboard calibration capabilities [9]. These advances allowed, for the first time, a near-true coloured visualisation of Earth from a geostationary point-of-view at unprecedented revisit frequencies [18].

The Advanced Himawari Imager (AHI) onboard Himawari-8/9 GEO satellite is currently providing diurnal meteorological observations over Australia, including the GBR. Himawari-8 is positioned at 140.7°E above the equator and with a 10 min scan rate, it captures at least 48 full-disk observations within a day (8 am to 4 pm local time). While the AHI instrument was designed for meteorological applications, its visible and near-infrared (VNIR) bands (Figure 1 and Table 1) enable the detection of marine features with strong optical signals, such as those from highly turbid waters [19–21]. In addition, Himawari-8 ultra-high temporal resolution observations allow the monitoring of ocean properties from sub-hourly to inter-annual time scales for the entire GBR lagoon and the adjacent oceanic basin without inter-orbital data gaps.

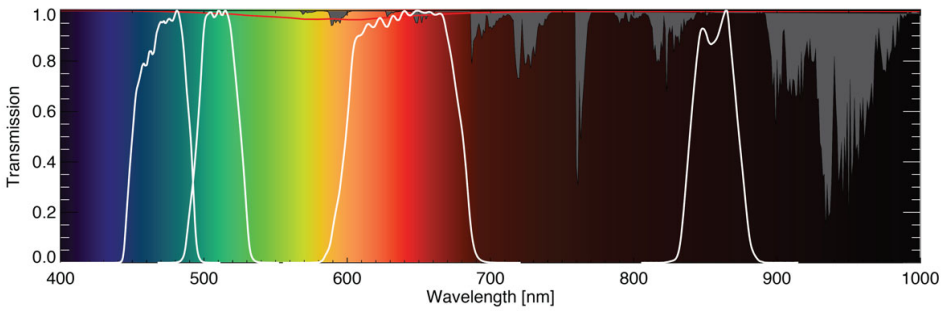

Figure 1. Himawari-8 spectral response functions of the visible and infrared bands (solid white lines) with the transmission of the atmospheric gases (grey filled line) and the transmission by ozone (red solid line) between 400 and 1000 nm.

An extensive range of applications for monitoring and management of oceanic areas have the potential to be derived from Himawari-8, including for ocean colour [22,23]. Recent studies have demonstrated the feasibility of Himawari-8 observations for detection of total suspended solids (TSS) in coastal waters [17,24] and for chlorophyll-a concentration (CHL) in the open ocean [22]. These results suggest an exciting opportunity for monitoring high-frequent and dynamic processes in the coastal GBR. However, although several ocean colour algorithms may be available for satellite retrieval of coastal water quality parameters, they may be unsuitable for the optical complexity of the GBR or not applicable to Himawari-8 observations.

Table 1. Himawari-8 Advanced Himawari Imager visible and near-infrared bands central wavelengths and bandwidth, associated spatial resolution. Signal-to-noise ratios (SNR) from performance test results [25].

Band # (Name)	Band Centre (Width)	Spatial Resolution	SNR @100% Albedo
#1 (blue)	470.64 (45.37) nm	1 km	585 (641.5)
#2 (green)	510.00 (37.41) nm	1 km	645 (601.9)
#3 (red)	639.15 (90.02) nm	0.5 km	459 (519.3)
#4 (NIR)	856.69 (42.40) nm	1 km	420 (309.3)

Model-based ocean colour algorithms that utilise radiative transfer simulations have shown superior performance for application in multi-temporal remote sensing studies of coastal waters compared to empirical algorithms [26]. Specifically, neural networks are a computationally efficient inversion method for remote sensing applications in optically complex coastal waters due to their capability to approximate non-linear functional relationships [27–35]. This paper describes the development of a model-based neural network ocean colour algorithm (Figure 2) for Himawari-8 and parameterised for the coastal waters of the GBR. The one-step inversion algorithm was developed to estimate TSS directly from Himawari-8 top-of-atmosphere (TOA) observations with a multilayer perceptron, a class of artificial neural networks (ANN). First, the spectral angular distribution of the TOA reflectances $\left(R_{TOA}(\lambda)\ \left[sr^{-1}\right]\right)$ was simulated at the VNIR Himawari-8 bands with an existing coupled ocean–atmosphere radiative transfer (RT) model (forward model). The RT simulations included realistic variations in water quality parameters, and atmospheric and illumination conditions. Several ANN experiments (inverse models) were then designed, trained, and tested to retrieve TSS at the Himawari-8 bands based on the simulated TOA radiances. Finally, the Himawari-8 retrieved TSS outputs were statistically assessed against concurrent in situ water quality data in the GBR and the limitations of the selected algorithm were investigated.

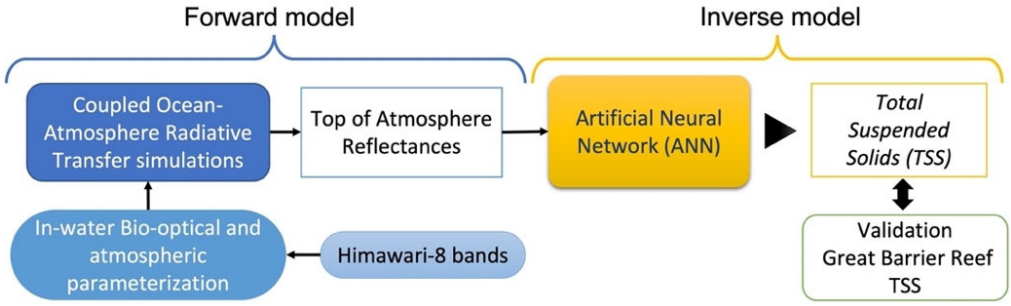

Figure 2. Flow diagram of the model-based ocean colour algorithm developed for Himawari-8.

2. Methods

The parameterisation of the radiative transfer simulations and the design of the ANN inverse model are specified in the following subsections. The forward and inverse model parameterisations follow an approach previously developed for European coastal waters [36–38] but were adapted in this study for the in-water optical conditions of the GBR [39]. Additionally, the Himawari-8 acquisition, processing and masking procedures, and the ocean colour processor are described for the model-based algorithm developed here. The validation protocol and methods for the assessment of the algorithm limitations are presented, as well as first results for TSS monitoring in the GBR.

2.1. The Forward Model

In this work, a scalar version of the Matrix-Operator MOdel (MOMO) [40,41] was employed for the coupled ocean–atmosphere radiative transfer simulations of the Himawari-8 VNIR bands (Table 1). Neglecting atmospheric polarisation may lead to errors of 1–2% at TOA, which is acceptable for coastal water applications [42]. The Himawari-8 $R_{TOA}(\lambda)$ were simulated for a realistic range of in-water and atmospheric optical properties of the GBR.

The simulated ocean–atmosphere system is stratified in several horizontally homogeneous plane-parallel layers where the defined types and concentrations of aquatic and atmospheric optical constituents are considered. The height of the simulated atmosphere (TOA) is 50 km thick and divided into 11 layers where the vertical profiles of pressure, temperature, and humidity follow a U.S. Standard Atmosphere [43]. The attenuation by Rayleigh scattering is accounted for with two barometric surface pressures of 980 hPa and 1040 hPa. The atmosphere is split into a boundary layer (0–2 km), a free troposphere (2–12 km), and a stratosphere (12–50 km). In each layer, the simulations were performed for eight distinct aerosol assemblages with varying concentrations of the aerosol optical thickness (τ_a) at 550 nm between 0.015 and 1.0. Each aerosol assemblage is composed of the three main aerosol models, a maritime model in the boundary layer, a continental model in the free troposphere, and a sulphuric acid model in the stratosphere, at a relative humidity between 70% and 99%. The τ_a range was determined from multi-annual Level 2 sun-photometer observations of the AERONET [44,45] station at the Lucinda Jetty Coastal Observatory (LJCO) located in the central GBR [18.52°S, 146.39°E]. Analysis of the corresponding Ångström coefficients [46] between 550 and 870 nm at the LJCO AERONET station confirm a mixture of maritime and continental aerosol types corresponding to those used in the RT simulations.

The transmission of atmospheric gases (except for O_3) were derived from the High-Resolution Transmission Molecular Absorption (HITRAN) database [47] and implemented in the radiative transfer simulations via the modified k-distribution model of Bennartz and Fischer [48]. The radiative transfer simulations were performed assuming a constant ozone loading of 344 Dobson Units (DU) [43]. The Himawari-8 bands were simulated for 17 solar and observation angles and 25 equally spaced relative azimuth angles. The simulations were conducted for realistic water quality fluctuations, represented by randomly selected unique concentrations of CHL, TSS, and yellow substances (YEL), hereafter referred to as concentration triplets. The ranges of the simulated concentration triplets were defined based on the dispersion of in situ correlated concentrations found in the GBR, following the approach by Zhang et al. [49]. The simulated concentration triplets were equally distributed in logarithmic space, so each order of magnitude was similarly represented while avoiding duplicated simulations.

The total spectral absorption of the sea water $a(\lambda)$ was modelled by a four-component bio-optical model accounting for the pure water absorption (a_w), the absorption of phytoplankton and all dead organic material (i.e., detritus) (a_{p1}) as a function of CHL [0.01, 15], the absorption of non-algal particles (a_{p2}) as a function of TSS [0.01, 100.0], and the absorption of yellow substances (a_y) at 443 nm [0.002, 2.5]. The absorption coefficient of pure water (a_w) was modelled according to Pope and Fry [50] for the Himawari-8 visible bands 1–3 and by Hale and Querry [51] for band 4. The spectral absorption of phytoplankton and detritus (a_{p1}) followed a parameterisation of Bricaud et al. [52], while the absorption of non-algal particles (a_{p2}) was parameterised according to Babin et al. [53], with a mean slope (S_{p2}) of 0.012 that was derived from in situ bio-optical data sampled in the GBR between 2002 and 2013. The spectral absorption coefficient of yellow substances (a_y) was modelled according to Babin et al. [53], with a mean slope S_y of 0.015 that was also derived from in situ observations from the GBR [39].

The total spectral scattering of the sea water $(b(\lambda))$ was modelled by a two-component bio-optical model [53] accounting for the scattering of pure water (b_w) and scattering or organic and inorganic particles (b_p) as a function of TSS. The pure seawater scattering

coefficient was expressed as a wavelength dependent power law based in Morel [54], defined for a global salinity average of 35 PSU. The scattering contribution of organic and inorganic particles was combined to derive the total particulate scattering coefficient (b_p) following the parameterisation of Babin et al. [55]. The mass specific scattering coefficient of TSS particles $\left(b_p^*\right)$ of 0.31 m^2 g^{-1} was calculated for the GBR waters, following Babin et al. [55]. A backscattering probability model for Case 2 waters was applied [49,56] to calculate and select the in-water scattering phase functions $\widetilde{\beta}(\theta, \lambda)$ based on the ratio of TSS and YEL. The simulations were performed for a large number of random concentration triplets and atmospheric conditions, as previously outlined, to build a comprehensive database of azimuthally resolved Himawari-8 $R_{TOA}(\lambda)$. From this database, statistically representative training and test subsets were randomly extracted to develop the inverse model. The training and test subsets each comprised 100,000 input vectors $\left(\vec{x}\right)$ containing the: simulated R_{TOA} at 470, 510, 640, and 856 nm bands, sea level atmospheric pressure between 980 and 1040 hPa, solar zenith angle (θ_s), observing zenith (θ_v), and relative azimuth $(\Delta\phi)$.

2.2. The Inverse Model

In this study, a multilayer perceptron (MLP), a class of feed-forward artificial neural network (ANN) [57], has been implemented as inverse model based on the Neural Network Simulator C-program developed by Malthouse [58], to approximate the functional relationship between the Himawari-8 $R_{TOA}(\lambda)$ and the TSS concentration. The present MLP comprises an input layer, a hidden layer, and an output layer of neurons. Each neuron is connected with each neuron of the next layer by a weight. The supervised machine learning or training procedure can be described as follows:

- The input neurons (n_i) receive the input vector $\left(\vec{x}\right)$, containing simulated reflectances and the ancillary data described above, and propagates it to the hidden layer neurons (n_h).
- In the hidden layer, the artificial neurons sum up the weighted input signals and pass these through a non-linear transfer function and subsequently forward their outputs to the output layer neurons (n_o).
- The cost function (i.e., mean squared errors, MSE—Equation (1)) between the simulated target outputs $\left(\vec{y}_t\right)$ and the ANN computed outputs $\left(\vec{y}_c\right)$ is calculated for the entire training dataset (N = 100,000), and the internal weights $(\boldsymbol{W_1}, \boldsymbol{W_2})$ of the network are adjusted.
- The training of the ANN is repeated until the cost function between output and target value is minimised.

$$\text{MSE} = \sum\left(\vec{y}_c - \vec{y}_t\right)/N \tag{1}$$

The cost function is minimised by adapting the weight matrices $(\boldsymbol{W_1}, \boldsymbol{W_2})$ iteratively using a Limited Memory Broyden–Fletcher–Goldfarb–Shanno optimisation algorithm [59]. For a three-layer MLP architecture, the complete analytic function is given by Equation (2):

$$\vec{y}_c = S_2 \times \left[\boldsymbol{W_2} \times S_1\left(\boldsymbol{W_1} \times \vec{x}\right)\right] \tag{2}$$

where S_1 and S_2 are the non-linear (Equation (3)) and linear transfer functions employed in the output and hidden layer, respectively.

$$S(x) = \left(1 + e^{-x}\right)^{-1} \tag{3}$$

The number of neurons in the input and output layers were determined by the number of input and output parameters of the problem, whereas several experimental attempts

were required to determine the optimal number of neurons in the hidden layer. The experiments were designed by varying the number of hidden layer neurons from 10 to 100, in increments of 10. A random but for all experiments fixed seed was used to initialise the weight configuration of the networks. The experiments included a principal component analysis (PCA) as a pre-processing step to decorrelate the $R_{TOA}(\lambda)$ inputs. In addition, the experiments were designed with 0.8% spectrally uncorrelated signal-dependent random noise added to the R_{TOA} inputs in each band. The ANN experiments were trained and tested with a subset of 100,000 input vectors randomly extracted from the radiative transfer simulated dataset. Each input vector was associated with a logarithmic TSS concentration, which was selected as the target output to be approximated by the supervised learning procedure. All experiments were trained for 1000 iterations and the minimisation of the cost function (Equation (1)) was computed over the entire training dataset at each iteration. An independent test dataset of N = 100,000 vectors was used to monitor the network training performance and to avoid over-fitting.

2.3. The Himawari-8 Ocean Colour Processing

Basic processing steps for Himawari-8 raw data into TSS products are shown in Figure 3. Level 1 (L1) full disk Himawari-8 VNIR bands were acquired, extracted over the GBR area (10 °S, 29 °S, 140 °E, 157 °E), geolocated, and navigation corrected. The geolocated raw data were transformed into Level 1b (L1b) TOA radiances ($L_{TOA}(\lambda)\left[\mathrm{W\ m^{-2}sr^{-1}\mu m^{-1}}\right]$) through the application of post-launch updated calibration coefficients [60]. The 640 nm band grid was resampled from 0.5 km to 1 km to match the resolution of the associated VNIR bands. The L1b calibrated $L_{TOA}(\lambda)$ were normalised by the extra-terrestrial solar irradiance $\left(F(\lambda)\left[\mathrm{W\ m^{-2}}\right]\right)$ for each band. $F(\lambda)$ was calculated as a function of the day of the year and using the mean extra-terrestrial solar irradiance $\overline{F}$ values based on Kurucz [61] and adapted to the Himawari-8 bands [62]. The resultant TOA reflectances $\left(R_{TOA}(\lambda)\left[sr^{-1}\right]\right)$ at the VNIR Himawari-8 bands served as inputs to the inversion method. In addition, the θ_s, θ_v, and $\Delta\phi$ values were calculated for each pixel of the satellite image as a function of latitude, longitude, and local time, following existing procedures [63], and converted into cartesian coordinates (x, y, z).

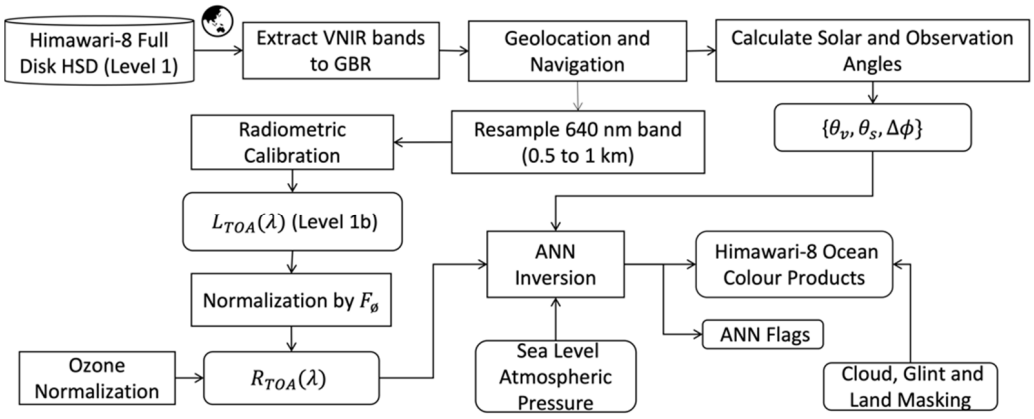

Figure 3. Himawari-8 Ocean Colour Processing flowchart. HSD refers to Himawari-8 Standard Data, GBR refers to Great Barrier Reef, VNIR refers to the Himawari-8 visible and near infrared bands (470, 510, 640, and 856 nm), and ANN refers to Artificial Neural Network.

Cloud masking of Himawari-8 observations was developed by Qin et al. [64] for the Australian continent and surrounding waters. The 2 km resolution cloud mask was resampled to the 1 km Himawari-8 grid and includes masking of pixels contaminated with dust and smoke plumes from biomass burning. Likewise, pixels identified as emerged surfaces, such as continental areas, islands, and shoals, were masked based on shapefiles available from the Great Barrier Reef Marine Park Authority [65] database. A sun-glint

mask was created by calculating the coordinates of the principal point of sun glint (PPS) as a function of the day of the year (solar inclination), local hour, latitude, and longitude [66], at 1 km spatial resolution. The contour of the sun disk was buffered for a circular radius of 1300 km from the coordinates of the PPS. The radius size was chosen after a series of visual tests were employed to ensure maximum coverage of the main sun disk area.

The Himawari-8 observations were normalised pixel-by-pixel and for each band with near-concurrent satellite data of total column ozone extracted from the Total Ozone from Analysis of Stratospheric and Tropospheric Satellite components (TOAST) product [67] prior to inversions. The TOAST product, with spatial resolution of 1.25 by 1 degrees and daily temporal resolution, was resampled to 1 km for compliance with the Himawari-8 grid. The Himawari-8 observations were normalised at each band by the ratio between the transmission of TOAST-derived ozone to the transmission of the simulated ozone column density of 344 DU. In addition, the mean sea level atmospheric pressure data from NCEP/NCAR 'Reanalysis 2' $\left(P_{atm}^{R2}\right)$ [68–70] were utilised as inputs for the inversion of Himawari-8 observations. The 'Reanalysis 2' data are averaged every 6 h (0, 6, 12, 18 UTC) and sampled on a regular global grid of 2.5 degrees spatial resolution [71]. The closest concurrent P_{atm}^{R2} data were acquired and resampled to the 1 km Himawari-8 grid. The retrieved TSS, associated masks, and metadata were saved in a NetCDF file, including pixel-wise associated flags for out-of-range inputs and outputs. The ranges of valid inputs and outputs were defined based on the RT simulated dataset. For instance, if a certain pixel input and/or output parameter exceeded the simulated ranges, the pixel was assigned a corresponding flag. The input and output flags were summed for each pixel of the Himawari-8 grid. The out-of-range flags were applied to the water quality products prior to the subsequent validation and application analyses.

2.4. Great Barrier Reef in Situ Data

In situ TSS measured between 2015 and 2018 by the Australian Institute of Marine Sciences (AIMS) and the Commonwealth Scientific and Industrial Research Organisation (CSIRO) were obtained from the IMOS Bio-optical Database [72] through the Australian Ocean Data Network (AODN) portal. Both CSIRO and AIMS use the gravimetric method to determine TSS concentration in seawater. The method consists of measuring the dry weight of suspended solids from a known volume of seawater sample after it has been vacuum filtered on a pre-weighted membrane filter. Further details on the methodology employed by AIMS and CSIRO are described in Great Barrier Reef Marine Park Authority [73] and Soja-Woźniak et al. [74], respectively. Despite AIMS and CSIRO laboratories using slightly different methods to determine TSS (i.e., number of replicates, filter pads, rinsing, etc.), these datasets have been combined in this validation exercise. A total of 347 in situ data points with TSS ranging from 0.01 to 85 mg L^{-1} and a mean of 3.5 mg L^{-1} were considered. In situ data points within 1 km from coastline or reefs were excluded from the analysis to reduce uncertainties due to adjacency effects [75]. We included all in situ seawater samples taken at the surface (<0.5 m depth) of stations located at variable water depths (1.5 m to 40 m), with the shallowest data point presenting TSS > 10 mg L^{-1}.

2.5. Validation Protocol

The validation protocol utilised in this study follows the experience of previous validation exercises for ocean colour remote sensing in Australia, including in the coastal GBR [27,76,77]. These studies described processing steps for extraction of satellite observations concurrent to in situ measurements in the coastal GBR, as well as useful statistical performance metrics.

Multiple Himawari-8 observations can be combined within a timeframe (i.e., hourly) to eliminate potential outliers and reduce sensor and environmental noise, likely improving estimates and validation performances [7,9,16]. Therefore, all available Himawari-8 observations scanned within ±30 min from the recorded in situ time were acquired for this validation exercise. Selected and processed 10 min Himawari-8 observations at the VNIR

bands with associated sun and observation geometry were subset to 3-by-3-pixel boxes, centred at the coordinates of each concurrent in situ data point. Likewise, 3-by-3-pixel subsets of concurrent masks (i.e., clouds, land, reefs, and sun glint) and ancillary data (i.e., ozone and pressure) were extracted. Near-true colour composites of selected Himawari-8 observations were visually inspected to eliminate matchups in waters with sharp horizontal gradients in optical properties (i.e., turbidity fronts) or nearby clouds.

Hourly composites of valid subsets were computed by temporal average, disregarding masked pixels. The hourly aggregated subsets were processed with the ANN inversion algorithms and masked for out-of-range values. Finally, the median and standard deviation of hourly TSS subsets were computed, excluding masked pixels. Only those subsets with two or less pixels masked per pixel-box were considered valid for matchup. The ANN outputs were computed in logarithmic scale (log10) and the concurrent in situ TSS was log-transformed for statistical analysis. An overview of the validation procedure is illustrated in Figure 4. The performances were evaluated with regards to their root mean square error (RMSE—or absolute error), bias, mean absolute percentage error (MAPE—or relative error), and the coefficient of determination (R^2). Bias, R^2, and RMSE were calculated in log10 space and MAPE was calculated in linear space, following Equations (4)–(7), where m is the measurement and p the satellite-derived product with N the number of valid matchups.

$$\text{RMSE} = \sqrt{1/N \sum (m-p)^2} \tag{4}$$

$$\text{MAPE} = 100/N \sum |(m-p)|/p \tag{5}$$

$$R^2 = \left[\frac{N(\sum mp) - (\sum m)(\sum p)}{\sqrt{\left[N\sum m^2 - (\sum m)^2\right]\left[N\sum p^2 - (\sum p)^2\right]}} \right]^2 \tag{6}$$

$$\text{Bias} = 1/N \sum (m-p) \tag{7}$$

The ANN match-up experiments were ranked based on the statistical metrics described above. Preference was given to those experiments with the lowest RMSE because this statistical parameter is the cost function that is minimised during the ANN training. The best-performing experiment with the lowest number of neurons in the hidden layer was selected, to reduce the computational efforts for the inversion of Himawari-8 observations over the entire GBR.

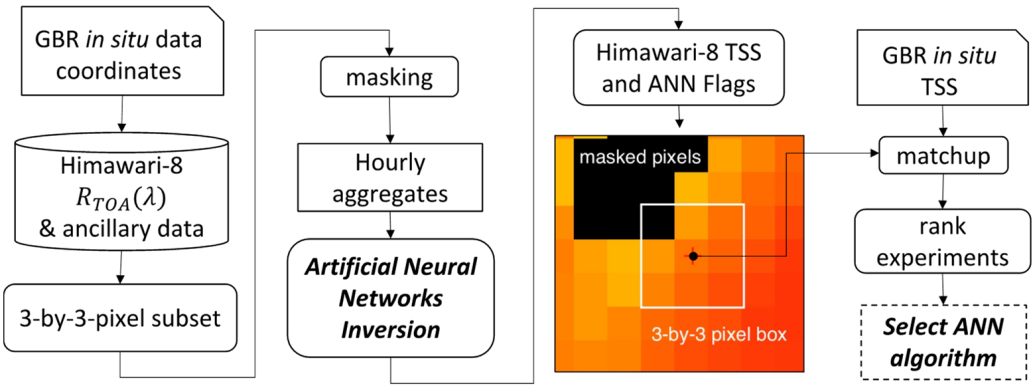

Figure 4. A simplified overview of the algorithm validation procedure.

2.6. Assessment of Limitations

The signal-to-noise ratios (SNR) were computed for the visible and near-infrared Himawari-8 $L_{TOA}(\lambda)$ observations scanned between 08:00 to 16:00 local time (Australian Eastern Standard Time—AEST) at selected dates and cloud-free areas of the Coral Sea

(16.25°S, 151°E and at 20.60°S, 153.53°E). Only post-July 2017 observations were considered for this analysis, given that their calibration coefficients were corrected for coherent and horizontal striping noise [63,78]. True colour snapshots available through the Himawari-8 Monitor P-Tree System [79] were browsed for target area selection and to ensure these were spatially uniform and unlikely to be influenced by clouds, sun glint, bio-optical features, and smoke plumes from terrestrial burning [80,81]. The selected Himawari-8 observations were converted from raw counts to physical units by applying calibration coefficients [60], with subsets of 51-by-51-pixels extracted and centred at the coordinates of the regions of interest. In addition, the subsets, associated masks, and geometric parameters were hourly aggregated. The 10 min and hourly aggregated subsets were masked for clouds, land, reefs, and sun glint, and their near-true colour composites were inspected for undetected features such as coral cays, reefs, cloud shadows, and sensor artefacts.

The SNR was calculated for each Himawari-8 band following Equation (8) [80]. Averaging $L_{TOA}(\lambda)$ for all valid pixels within the target area gives $L_{typical}(\lambda)$, and taking the standard deviation (σ) within the same area gives the noise equivalent radiance ($L_{noise}(\lambda)$). The SNR is calculated as the ratio between $L_{typical}$ and L_{noise} at each band:

$$\mathrm{SNR}(\lambda) = L_{typical}(\lambda)/L_{noise}(\lambda) = \overline{L}_{TOA}(\lambda)/\sigma(L_{TOA}(\lambda)) \quad (8)$$

The diurnal variability and magnitude differences between SNR computed with 10 min and hourly aggregated Himawari-8 observations ($\mathrm{SNR}_{SING}(\lambda)$ and $\mathrm{SNR}_{AGG}(\lambda)$, respectively) were inspected at each band. In addition, their spectral characteristics were evaluated for ranges of θ_s because noise levels are known to vary with solar elevation [80]. Finally, the associated percentage noise levels ($\%Noise$) were computed for $\theta_s = 45° \pm 1°$ and utilised to evaluate the algorithm's sensitivity to Himawari-8 typical noise levels.

The TSS algorithm developed in this study was trained with spectrally flat (uncorrelated) photon noise (0.8%) that was added to the training dataset, assuming limited knowledge of sensor performance characteristics over oceanic targets. To evaluate the inversion stability and to provide a baseline sensitivity analysis of the TSS algorithm, spectrally flat photon noise of 0.1, 1.0, and 10 and 50% were added to the testing dataset and inverted. In addition, the $\%Noise$ associated with the Himawari-8 bands were added to the testing dataset to quantify the effects of spectrally dependent noise levels on the accuracy of TSS retrievals. The retrieval stability was interpreted in terms of constant increments of RMSE across a wide range of TSS (0.01 to 100 mg L^{-1}) equally spaced in logarithmic concentrations. In addition, longitudinal transects of TSS products taken in homogeneous and cloud-free waters of the coastal GBR and in the Coral Sea were evaluated at a pixel scale for a qualitative assessment of noise levels of Himawari-8.

3. Results

3.1. Algorithm Validation

Multiple networks were trained with varied architecture configurations and the best-performance network with lowest possible RMSE and lowest number of neurons in the hidden layer was selected for inversions. The selected experiment, with 50 neurons in the hidden layer, retrieved TSS ranging from 0.14 to 24 mg L^{-1}, with a positive R^2 and bias of 0.014 mg L^{-1}, MAPE of 75.5%, and 10^{RMSE} of 2.08 mg L^{-1}, as shown in Figure 5.

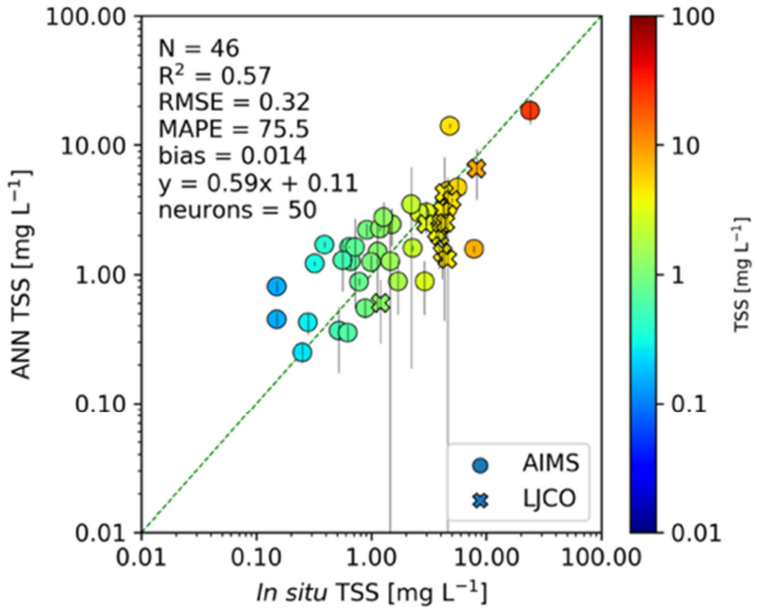

Figure 5. In situ and Himawari-8-derived TSS with the best-performing ANN experiment, with in situ TSS values colour-coded in logarithmic scale. Error bars represent the intra-pixel standard deviation of TSS within a 3-by-3-pixel box. Different symbols indicate in situ data collected by AIMS and by CSIRO at LJCO.

3.2. Himawari-8 Total Suspended Solids for the Great Barrier Reef

Figure 6 shows a near-true colour composite of Himawari-8 (left panel) taken on 27 October 2017 over the GBR area, and the corresponding TSS product at 10 min temporal resolution (right panel). The waters within the GBR lagoon have TSS generally at or above 1 mg L^{-1}, whereas the waters offshore the GBR present values below 1 mg L^{-1}. The TSS product revealed severe granulation and striping noise in the open ocean areas of the Coral Sea.

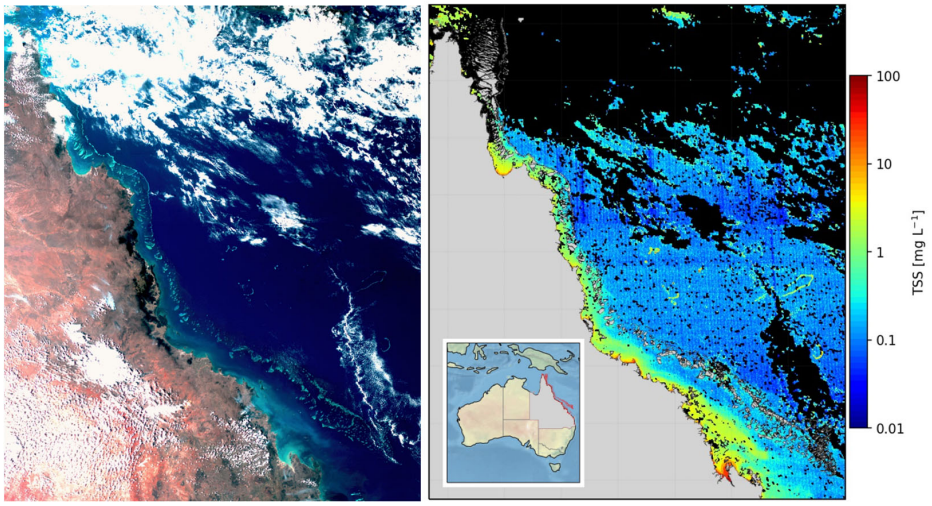

Figure 6. Near-true colour Himawari-8 imagery of the GBR acquired on 27 October 2017 at 15:00 AEST (**left panel**) and the associated TSS product [mg L^{-1}] (**right panel**). Pixels masked in black due to clouds and out-of-range values.

Himawari-8 TSS fluctuations were investigated for the coastal waters surrounding the Burdekin River mouth and over the southern GBR reef matrix (Figure 7 and animations in link). The Burdekin flood event of 12 February 2019 generated a sediment plume that reached the outer reefs (50 km from the mouth) between 3 to 4 pm, with TSS > 20 mg L^{-1}.

The Burdekin River sediment plume developed during the incoming tide with a range of 0.3 m between low and high tide. The coastal waters near the reefs experienced an order magnitude increase in TSS (3.6, 26.4 mg L^{-1}) within a semi-diurnal tidal cycle (cross mark in Figure 7 (left panel) and Figure 8a). The reefs covered by floodwaters were exposed to TSS ~40 times higher than the guideline threshold of 0.7 mg L^{-1} [82]. The areas where TSS exceeded 100 mg L^{-1}, near the mouth, were masked (black areas) as out-of-range values (ANN flags). An animation of the TSS fluctuations following the main discharge event is available in Figure S1.

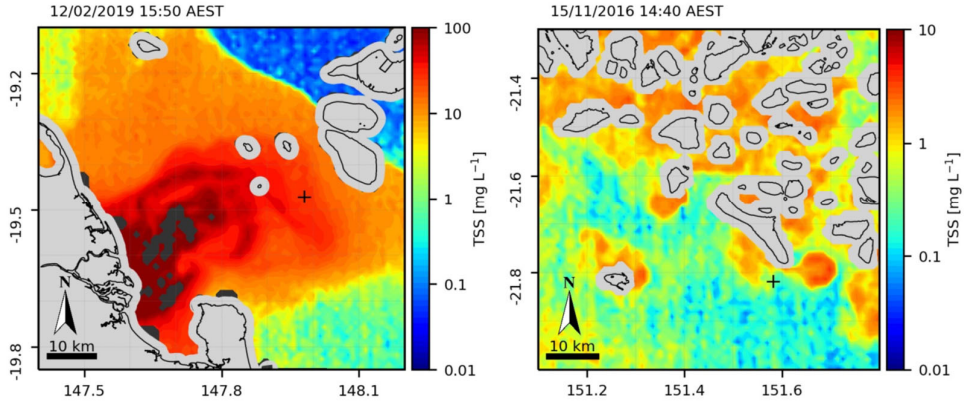

Figure 7. Flood plume discharging from the Burdekin River, February 2019 (**left panel**). TSS tidal jets within the GBR reef matrix in November 2016 (**right panel**). Note the different ranges in each plot. Pixels masked in black are due to out-of-range TSS values.

While major flood events display clear TSS features in the coastal GBR, sub-mesoscale tidal jets are observed surrounding the matrix of shallow and submerged reefs in the southern GBR (Figure 7 (right panel)), demonstrating how these different conditions both influence short-term TSS variability. The animation provided in Figure S2 illustrates the dynamics of tidally induced TSS fluctuations, where the high (4 m) and low (0.2 m) tides took place at 10 a.m. and 6 p.m., respectively (Figure 8b). The TSS concentrations near Heralds Reef (cross marked) fluctuated about one order in magnitude within a day (0.3, 2.0 mg L^{-1}), with values exceeding the water quality guideline thresholds recommended for the open coastal GBR (0.7 mg L^{-1}).

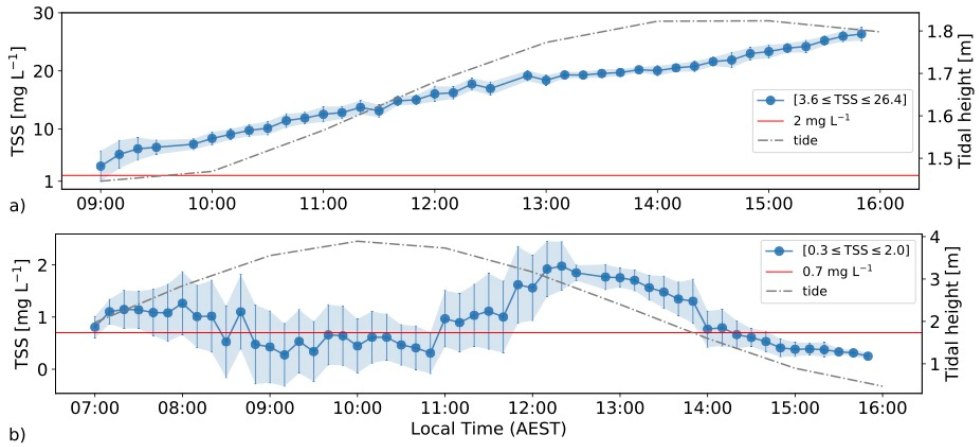

Figure 8. Time series of 10 min Himawari-8-derived TSS at the mouth of the Burdekin River during the floods of February 2019 (**a**) and in the southern GBR reef matrix in November 2016 (**b**), as shown in Figure 7. Error bars represent intra-pixel standard deviations. Guideline thresholds for inshore (2.0 mg L^{-1}) and mid-shelf (0.7 mg L^{-1}) waters are marked in red. Note the different time ranges in each figure.

3.3. Detection Limits

The SNR computed from two sets of Himawari-8 observations are shown in the graphics of Figure 9. A few single observations were missed due to intensive cloud coverage, particularly on 06 September 2017, and resulted in data gaps in the time series. SNR_{SING} and SNR_{AGG} presented clear diurnal fluctuations, with the highest SNR occurring at the lowest θ_s (<30°), between 11 a.m. and 12 p.m. The magnitude and diurnal variability were higher for SNR_{AGG} and at the blue and green bands (470 and 510 nm), when compared to values computed for SNR_{SING}. The SNR calculated for the 640 nm and 856 nm bands were at least three times lower than the SNR computed for the blue and green bands, with subtle diurnal variations. The diurnal fluctuations of SNR between days and locations were varied, especially for the blue band and from SNR_{AGG}. On 06 September 2017 (mean θ_v~22°), the SNR_{AGG} in the blue and green bands were similar in magnitude (Figure 9b). On 25 September 2017 (at a different location with mean θ_v~28°), the blue band presented SNR_{SING} nearly twice as high as the green band (Figure 9d).

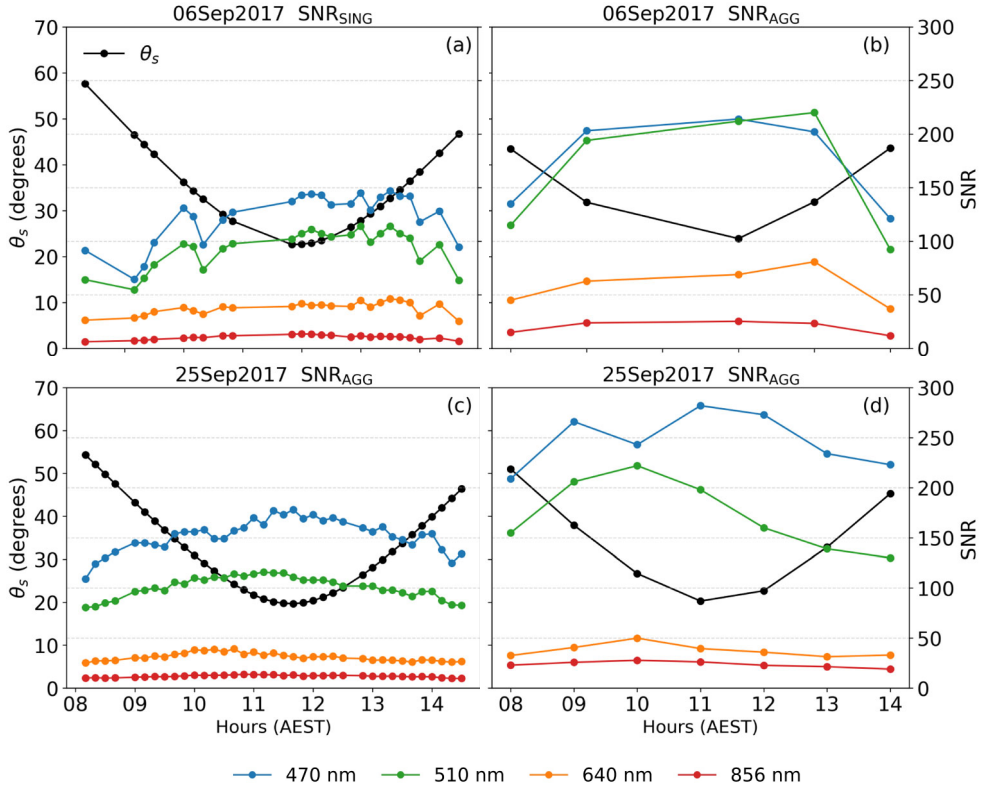

Figure 9. Time series of signal-to-noise ratios (SNR, right axis) computed for single (SNR_{SING}) (**a**,**c**) and for aggregated (SNR_{AGG}) observations (**b**,**d**) with associated θ_s (left axis). The SNR is colour-coded by band.

The spectral variability of SNR_{SING} and SNR_{AGG} is shown in Figure 10 for three groups of θ_s, where the standard deviations within each group were plotted as capped error bars. The single observations typically yielded lower SNR than the aggregated observations in all bands, and SNR was the highest for $\theta_s < 30°$, in agreement with the data presented in Figure 9. The standard deviations of SNR computed for single and aggregated observations were more pronounced for $\theta_s > 40°$ and at the blue and green bands. The SNR calculated for $\theta_s > 40°$ at the blue band presented standard deviations of 27 and of 51 for SNR_{SING} and SNR_{AGG}, respectively, while the SNR computed for the green band presented standard deviations of 13 and 26, respectively. These deviations are likely associated with the variable atmospheric conditions of each location, which are intensified at the blue and green bands and at high atmospheric pathlengths.

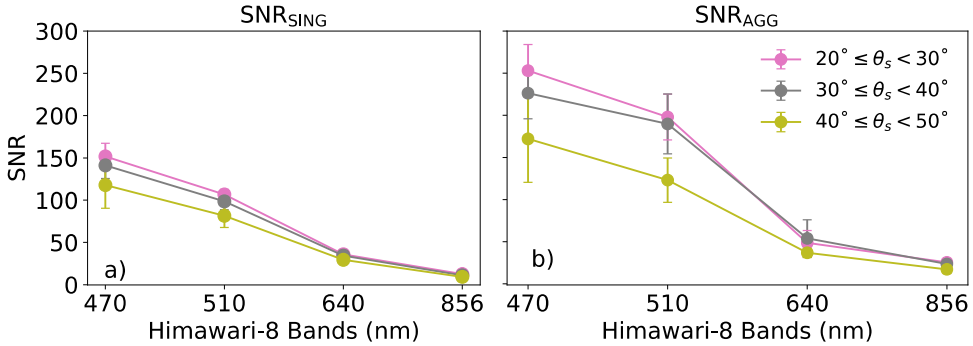

Figure 10. Spectral distribution of signal-to-noise ratios calculated for single (SNR_{SING}) (**a**) and aggregated observations (SNR_{AGG}) (**b**), and grouped for three ranges of θ_s. Error bars were computed as standard deviations of SNR within each group of θ_s.

The SNR_{AGG}, the $L_{typical}$, and L_{noise} and associated percentage noise (*%Noise*) for aggregated observations with $\theta_s = 45° \pm 1°$ were compiled in Table 2. Likewise, the SNR_{SING} computed for all single observations with $\theta_s = 45° \pm 1°$ were included for comparison. The SNR_{AGG} values compiled in Table 2 were about twice as high as the corresponding SNR_{SING}, except in the red band. Nevertheless, the large noise levels in the red (~3%) and in the NIR bands (~5%) indicate that the SNR_{AGG} may be mostly affected by the atmospheric signal despite the efforts in avoiding environmental conditions in image selection. This is particularly evident in the NIR band, where the water leaving radiances are considered negligible in clear open ocean waters.

Table 2. Visible and near-infrared Himawari-8 $L_{typical}$ and L_{noise} $\left(W\ m^{-2}sr^{-1}\mu m^{-1}\right)$ and associated percentage noise (*%Noise*) for SNR_{AGG} at $\theta_s = 45° \pm 1°$. Calculated SNR_{SING} at $\theta_s = 45° \pm 1°$ values were added for comparison.

Band	$L_{typical}$	L_{noise}	*%Noise*	SNR_{AGG}	SNR_{SING}
470	59.5	0.26	0.44	223	100
510	38.3	0.29	0.76	130	74
640	13.8	0.41	3.02	33	28
865	3.4	0.18	5.26	19	8

The outcomes of retrieving TSS (0.01 to 100 mg L^{-1}) with spectrally flat and spectrally dependent photon noise is illustrated in the graphics of Figure 11. In both scenarios, the algorithm presents reasonable retrieval performances for TSS at or above 0.1 mg L^{-1}, except when 50% of spectrally flat photon noise is added to the Himawari-8 bands (Figure 11a). Meanwhile, large errors (>300%) were obtained for TSS retrievals below 0.1 mg L^{-1}, irrespective of noise type and level. On a more realistic scenario, when spectrally dependent photon noise (i.e., *%Noise* from Table 2) is added to the Himawari-8 bands, the errors are mostly below 100% for TSS > ~0.25 mg L^{-1} (Figure 11 (right panel)). Therefore, for obtaining reliable retrievals from Himawari-8 with the current TSS algorithm, a detection limit of 0.25 mg L^{-1} was chosen. For comparison, the detection limits of TSS retrievals computed from atmospherically corrected Himawari-8, as in Dorji and Fearns [17], is represented as a vertical dashed line at 0.15 mg L^{-1}.

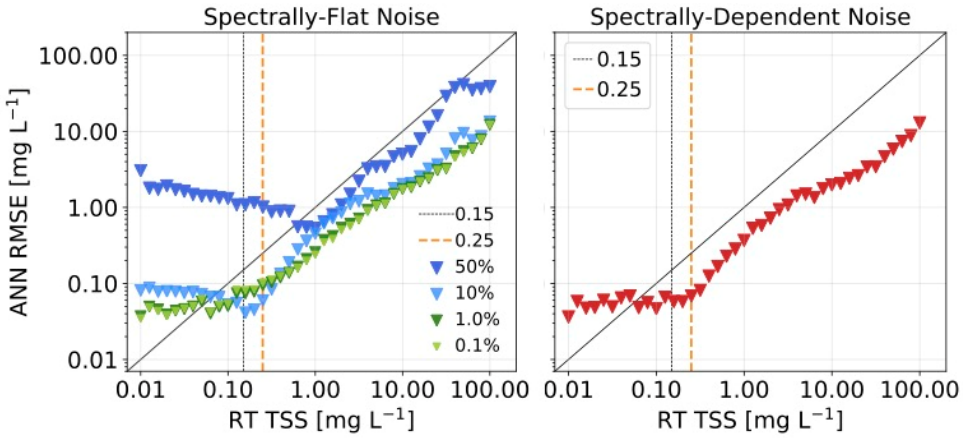

Figure 11. Retrieval RMSE errors (in mg L^{-1}) for spectrally flat (**left panel**) and spectrally dependent (**right panel**) photon noise levels. Radiative transfer (RT) TSS and associated RMSE values are presented in logarithmic scale. The vertical dashed line at 0.15 mg L^{-1} is the detection limit adapted from Dorji and Fearns [17], 2018. The vertical dashed line at 0.25 mg L^{-1} is the detection limit of the present method.

A visual inspection of noise levels revealed severe granulation and horizontal stripes in Himawari-8 TSS products (Figure 12), particularly when TSS was obtained from a single observation (TSS_{SING}) and in open ocean waters (TSS < ~0.1 mg L^{-1}). The intensity of granulation was severely reduced in aggregated TSS product (TSS_{AGG}) and negligible in turbid coastal areas (TSS > ~1 mg L^{-1}). In addition to reducing granulation and noise, the TSS_{AGG} showed increased masking around cloud-persistent areas. The longitudinal transects of TSS_{SING} and TSS_{AGG} taken between 151°E and 152°E in the coastal GBR and in the Coral Sea (magenta arrows, Figure 12) are illustrated in time series in Figure 13.

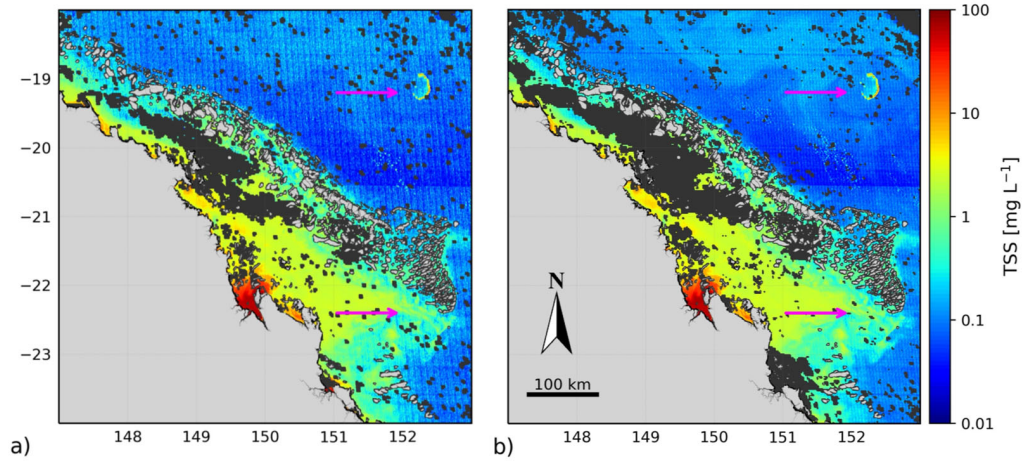

Figure 12. Location of transects (magenta arrows) extracted for TSS_{SING} (**a**) and TSS_{AGG} (**b**). Note the cumulative cloud masking in TSS_{AGG}. Himawari-8 observations taken on 9 September 2017 between 10:00 and 10:50 local time (AEST).

The transect sampled between 19°S and 20°S in the Coral Sea (Figure 13a) presented TSS_{SING} and TSS_{AGG} values mostly below the detection limits of the method (0.25 mg L^{-1}), which may present retrieval errors over 100%. TSS_{SING} presented spikes or different orders of magnitude values occurring successively on a pixel scale (or within 1 km). As a result, differences of up to 0.3 mg L^{-1} were observed between neighbouring pixels, as indicated by plot annotations in Figure 13a. Meanwhile the associated TSS_{AGG} presented smoother pixel-to-pixel variations (~0.06 mg L^{-1}). Subtle differences were observed

between TSS_{SING} and TSS_{AGG} in the transects taken in the coastal GBR (Figure 13b), particularly for TSS > 1 mg L^{-1}. However, with increasing distance from the coast, TSS dropped below 1 mg L^{-1} and differences between TSS_{SING} and TSS_{AGG} were enhanced. Although most TSS_{SING} pixels of Figure 13b were above detection limits (0.25 mg L^{-1}), they presented poor spatial coherency in the coast-to-ocean transition area (151.4° to 152.0°E). Because TSS_{SING} and TSS_{AGG} provide comparable results for TSS > ~1 mg L^{-1}, both may be appropriate for monitoring the coastal GBR. However, TSS_{AGG} presents overall better spatial coherency and may be preferred over TSS_{SING}, depending on the area of application.

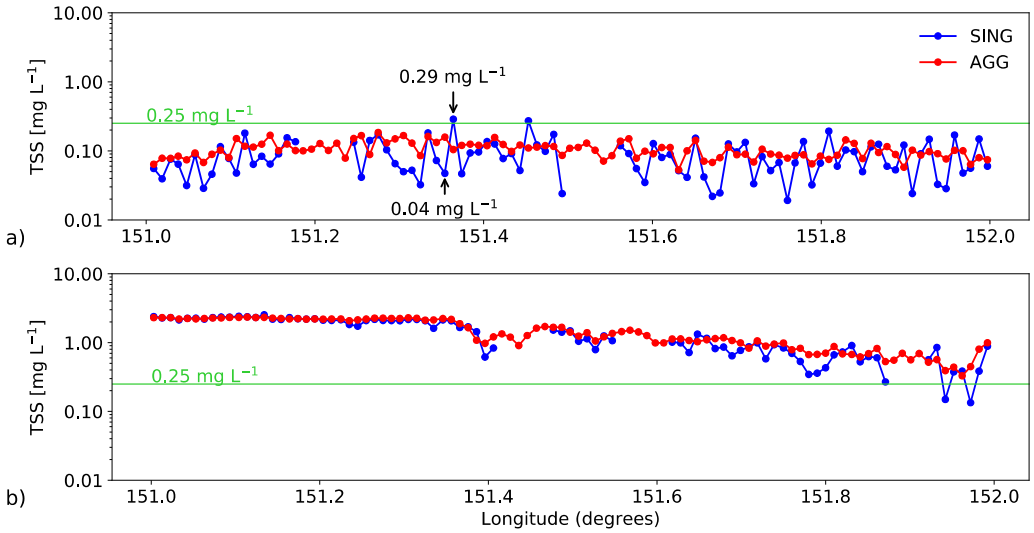

Figure 13. Transects of Himawari-8-derived TSS (mg L^{-1}) taken in the Coral Sea (**a**) and within the coastal GBR waters (**b**) from TSS_{SING} (blue dots) and TSS_{AGG} (red dots). The data gaps represent pixels masked for clouds, land, sun glint, or ANN flags, where appropriate. The annotated TSS (in black arrows) indicate pixel-to-pixel values and the green horizontal line marks the detection limit of the method.

4. Discussion

Synoptic monitoring of water quality in the extensive and optically complex GBR is a priority, presenting a challenge for environmental managers and researchers [2,83]. Although ocean colour remote sensing has stringent radiometric and spectral requirements, Himawari-8 offers an unprecedented number of observations for the advanced water quality monitoring of the GBR. This paper presents the first advanced remote sensing algorithm locally tuned and validated for the synoptic monitoring of water quality at diurnal scales in the GBR.

4.1. Algorithm Development and Validation

The coupled ocean–atmosphere radiative transfer simulations provided a large and robust database of R_{TOA} distribution in the Himawari-8 VNIR bands, parameterised for the optical variability of the GBR. The machine learning ANN algorithm developed in this work allowed the direct inversion of R_{TOA} to derive a wide range of TSS values (0.01 to 100 mg L^{-1}), without an explicit atmospheric correction procedure. This presents an advantage compared to traditional methods based on the inversion of water-leaving reflectances, in which the accuracy of the final inversion is subject to the accuracy of the atmospheric correction [27,36,37,84]. Despite Himawari-8 spectral limitations, the ANN retrievals compared well with target outputs from simulated testing datasets and provided confidence in the quality of the trained algorithms. Moreover, the algorithm's robustness to input noise was especially advantageous considering Himawari-8 does not meet the minimum radiometric requirements of ocean colour sensors and environmental noise, particularly from the atmosphere, can largely impact the retrievals. These results

encouraged further application of Himawari-8 observations for validation against in situ water quality data in the GBR.

The retrieved Himawari-8 TSS matchup errors compared well with the mission targets defined for other ocean colour sensors, such as Sentinel-3 in Case 2 waters [85], particularly for TSS above 0.1 mg L^{-1}. The performance of the present algorithm compares well with those using atmospherically corrected Himawari-8 observations [17,24], indicating the suitability of deriving coastal TSS with model-based one-step inversions. Explicit atmospheric correction procedures may improve retrievals for the lower TSS range (<~1 mg L^{-1}), which are likely affected by the dominating atmospheric path radiance and the low radiometric performance of Himawari-8.

Performance improvements would require a larger and more comprehensive database of in situ bio-optical measurements covering the relevant spatial and temporal scales of variability. Moreover, rigorous measurement protocols need to be followed for reducing uncertainties associated with algorithm parameterisation and validation in coastal waters. For instance, triplicate samples are recommended for the determination of TSS with the gravimetric method. In addition, validation samples should be taken in optically homogeneous waters [86], which is especially difficult in highly dynamic coastal settings. Nevertheless, in situ measurements have been made available by multiple research agencies with diverse scientific priorities employing distinctive sampling and analysis methods. In addition, physical and environmental processes, such as bottom reflectance, fluorescence, bidirectional reflectance, polarisation, and harmful algal blooms, were not accounted for but may also contribute to the matchup retrieval errors.

4.2. Himawari-8 Total Suspended Solids for the Great Barrier Reef

Himawari-8 allowed the near-real time monitoring of an episodical flood event in the GBR, revealing an order magnitude TSS increase within a day. This event was observed during a wet season where the Burdekin discharged between 0.5 and 1.5 million ML/day for 10 consecutive days (Burdekin River at Clare station [87]). TSS fluctuations from the Burdekin flood plume were well above the water quality guideline threshold value of 2 mg L^{-1} for open coastal and mid-shelf waters, as well as 0.7 mg L^{-1} for offshore waters of the GBR [82]. The flood plume extended 50 km into the outer reefs, and its diurnal development was followed step-by-step with 10 min Himawari-8-derived TSS. Therefore, Himawari-8 provided an unprecedented number of observations for a complete qualitative and quantitative monitoring of flood events in the GBR. The masked pixels in floodwaters indicate values beyond 100 mg L^{-1}, implying that the simulation range should be expanded for values above this limit for retrievals during floods in the GBR.

The TSS features in the southern reef matrix are likely resultant from short-lived sub-mesoscale resuspension eddies (1–10 km diameter), often referred to as tidal jets. In the southern GBR, large tidal ranges (5–10 m) induce strong currents [88,89], pushing water through narrow and relatively shallow channels [90]. These complex hydrodynamics promote the resuspension and injection of TSS from the shelf break into the reef matrix, and TSS concentrations in these regions are likely independent of terrestrial sources [91]. The tidal jets have been associated with localised upwelling and nutrient exchange between the Coral Sea and the GBR lagoon [92,93], being an important mechanism of transport and mixing of sediments, nutrients, and phytoplankton production [94]. However, the location and occurrence of tidal jets are scarcely described due to lack of appropriate spatial and temporal resolution observations [95,96]. Himawari-8 allowed the identification and tracking of such features within the GBR, at the required temporal resolution for resolving short-lived coastal processes.

4.3. Limitations

Himawari-8 provides inferior SNR compared to past and currently operational ocean colour sensors [80], and its sensitivity is far below minimum requirements for ocean colour applications, particularly over open ocean waters [9,97]. However, Himawari-

8's moderate radiometric resolution of 11 bits is unlikely to saturate over bright targets, such as clouds [80], and over extremely turbid coastal waters (TSS ~100 mg L^{-1}), while yielding enough sensitivity to provide a reasonable level of discretisation over clear waters (>0.25 mg L^{-1}). Noise levels calculated from aggregated observations were generally lower than those from single observations in all bands, confirming the suitability of degrading the temporal resolution to improve image quality [7,16]. Despite diurnal SNR fluctuations being largely modulated by solar elevation angles, the spectral dependence implies that a considerable source of input noise (3–5% in the red and NIR bands) in open ocean waters may originate from the atmosphere [80]. Nevertheless, the detection limit of the present method (0.25 mg L^{-1}) is comparable to those employing explicit atmospheric correction to the inversion of meteorological data [17,98].

The detection limit of 0.25 mg L^{-1} is close to the detection limit of in situ TSS measured with the gravimetric method of ~0.4 mg L^{-1}, for AIMS and CSIRO. Relative uncertainties of the gravimetric method are associated with the measurement protocol employed by different laboratories, which include differences in filter types, operator bias, salt rinsing, etc. [99,100]. For instance, salt crystals trapped in glass fibre filters largely affect TSS measurements and salt should be removed by rinsing the filtration apparatus [101,102]. Yet, errors as large as 30% have been obtained employing different salt-rinsing techniques, hindering the accurate determination of TSS lower than 1 mg [101]. Therefore, the detection limits and relative uncertainties of in situ measurements and Himawari-8-derived TSS are comparable for the present study. This result suggests that Himawari-8 offers an opportunity to accurately monitor diurnal variability of water quality in the coastal GBR, for TSS between 0.25 and 100 mg L^{-1}.

Himawari-8-derived TSS products presented a systematic horizontal striping, with size generally corresponding to individual horizontal scans (500 km), as previously identified by Murakami [22]. The striping resulted from differences in detector-to-detector calibration slopes from solar diffuser observations of the visible bands [103,104]. Although the calibration coefficients were applied for the post-July 2017 observations, the horizontal striping patterns were still present in offshore waters and with TSS < 1 mg L^{-1}. Additionally, severe granulation was observed in TSS products derived every 10 min, potentially associated with the low radiometric performance of the Himawari-8 sensor over water targets [17,22]. However, the visual noise was largely reduced by temporal aggregation of several individual observations into hourly-derived TSS products [16]. Fortunately, granulated noise was negligible in coastal and moderately turbid waters (TSS > 1 mg L^{-1}), either from 10 min or from hourly TSS products. This result may be associated with the increased backscattering of suspended particles, which increases the water-leaving radiance and overwhelms the photon noise [105]. Consequently, Himawari-8-derived TSS is more likely to be accurately retrieved over moderately turbid coastal waters than over the open ocean, corroborating the detection limits analysis.

Pixel-to-pixel variations in open ocean areas (TSS < 0.25 mg L^{-1}) were likely related to the granulated patterns observed with visual inspection, due to the low sensitivity of the Himawari-8 sensor at 10 min resolution. The radiometric noise for TSS below 0.25 mg L^{-1} were largely reduced in aggregated TSS, corroborating the sensitivity and visual inspection analyses. Conversely, improved spatial coherency was observed in the coastal GBR transect for TSS > 1 mg L^{-1}. As a result, Himawari-8 10 min-derived TSS can be utilised with as much confidence as TSS derived from hourly aggregated observations in coastal areas. Obtaining TSS at every 10 min in the coastal GBR improves the discrimination of rapid-changing water quality fluctuations within an hour. However, this near-real time temporal frequency requires large processing and storing capabilities that may be unfeasible for the entire GBR. Producing hourly TSS, otherwise, not only improves processing rates and storage capabilities but also helps eliminate outliers and increase the accuracy of TSS products.

5. Conclusions and Future Perspectives

In-situ monitoring and LEO satellite data have provided much of our knowledge on flood plumes entering the GBR [4,106–108]. However, infrequent and spatially scant observations hindered the full understanding of plume development and evolution over short time scales. This study demonstrated the suitability of Himawari-8 for reliable TSS retrievals in the coastal GBR and for flood plumes mapping, tracking, and monitoring. For the first time, coastal TSS features were reliably quantified for the entire GBR, at rates only possible with biogeochemical and hydrodynamic models [109]. Himawari-8 TSS products brings forth the ability to characterise and resolve periodical and short-lived phenomena at unprecedented spatiotemporal resolutions. These products will be useful for researchers, modellers, and stakeholders assessing the impact of water quality in GBR ecosystems currently only using LEO orbit ocean colour products [109]. Diurnal changes and drivers of water quality fluctuations should be further investigated in the GBR using Himawari-8 TSS products and data of coastal processes such as tides, winds, and freshwater discharge. Additionally, the algorithm presented in this study can be directly employed to the identical Himawari-9 AHI sensor, which is planned to succeed Himawari-8 by 2029. The next-generation Himawari mission (Himawari-10) is in the planning phase and additional channels in the visible range, as well as improved sensitivity and spatial resolution, are a possibility. These characteristics would largely advance the capabilities of ocean colour algorithms for geostationary sensors, allowing more accurate retrievals in coastal waters at diurnal scales. Likewise, the Advanced Meteorological Imager (AMI) on board the GEOKOMPSAT-2A, as well as the GOCI-II (GEOKOMPSAT-2B), are currently observing Australia and East Asia, and a similar machine learning algorithm could be developed for harnessing these large and abundant datasets in near-real time. In this context, the present study provides an advanced algorithm and a prospect of potential applications to be developed when ocean colour sensors onboard geostationary platforms become a reality for Australia.

Supplementary Materials: The following are available online at https://www.mdpi.com/article/10.3390/rs14143503/s1, Figure S1: Diurnal variability of Total Suspended Solids over the Burdekin River mouth in February 2019 from 10 min Himawari-8 observations, Figure S2: Diurnal variability of Total Suspended Solids over the Southern Great Barrier Reef near Heralds Reef in November 2016 from 10 min Himawari-8 observations.

Author Contributions: Conceptualization, L.P.-V. and T.S.; methodology, L.P.-V. and T.S.; software, L.P.-V., T.S. and Y.Q.; validation, L.P.-V.; formal analysis, L.P.-V.; data curation, L.P.-V., T.S. and Y.Q.; writing—original draft preparation, L.P.-V.; writing—review and editing, T.S., M.J.D., S.S. and Y.Q.; supervision, T.S., M.J.D. and S.S.; funding acquisition, L.P.-V. All authors have read and agreed to the published version of the manuscript.

Funding: This research was funded by the National Council for Scientific and Technological Development (CNPq) Foundation of the Brazilian Federal Government through the Sciences without Borders Program, grant number 206339/2014-3.

Data Availability Statement: The data presented in this study are available on request from the corresponding author.

Acknowledgments: We acknowledge Juergen Fischer and Michael Schaale (Institute of Space Sciences, Department of Earth Sciences, Freie Universität Berlin) for providing access to the MOMO radiative transfer code and for the inverse modelling tool. Britta Schaffelke, Michele Skuza, and Renee Gruber (AIMS) are acknowledged for providing valuable in situ data collected as part of the Marine Monitoring Program for Inshore Water Quality, a collaboration between the Great Barrier Reef Marine Park Authority, the Australian Institute of Marine Science, James Cook University, and the Cape York Water Monitoring Partnership. The Japan Meteorological Agency is acknowledged for the operation of Himawari-8 and data distribution through the Australian Bureau of Meteorology. The Australian Bureau of Meteorology is acknowledged for providing tidal prediction data. In situ data were sourced from Australia's Integrated Marine Observing System (IMOS)—IMOS is enabled by the National Collaborative Research Infrastructure Strategy (NCRIS). NCRIS (IMOS) and CSIRO

are acknowledged for funding the Lucinda Jetty Coastal Observatory. This research was undertaken with the assistance of resources from the National Computational Infrastructure (NCI Australia), an NCRIS-enabled capability supported by the Australian Government.

Conflicts of Interest: The authors declare no conflict of interest.

References

1. Schroeder, T.; Devlin, M.J.; Brando, V.E.; Dekker, A.G.; Brodie, J.E.; Clementson, L.A.; McKinna, L. Inter-annual variability of wet season freshwater plume extent into the Great Barrier Reef lagoon based on satellite coastal ocean colour observations. *Mar. Pollut. Bull.* **2012**, *65*, 210–223. [CrossRef]
2. Devlin, M.; Petus, C.; da Silva, E.T.; Tracey, D.; Wolff, N.; Waterhouse, J.; Brodie, J. Water Quality and River Plume Monitoring in the Great Barrier Reef: An Overview of Methods Based on Ocean Colour Satellite Data. *Remote Sens.* **2015**, *7*, 12909–12941. [CrossRef]
3. Blondeau-Patissier, D.; Brando, V.E.; Lønborg, C.; Leahy, S.M.; Dekker, A.G. Phenology of Trichodesmium spp. blooms in the Great Barrier Reef lagoon, Australia, from the ESA-MERIS 10-year mission. *PLoS ONE* **2018**, *13*, e0208010. [CrossRef] [PubMed]
4. Petus, C.; Waterhouse, J.; Lewis, S.; Vacher, M.; Tracey, D.; Devlin, M. A flood of information: Using Sentinel-3 water colour products to assure continuity in the monitoring of water quality trends in the Great Barrier Reef (Australia). *J. Environ. Manag.* **2019**, *248*, 109255. [CrossRef]
5. Brodie, J.; Schroeder, T.; Rohde, K.; Faithful, J.; Masters, B.; Dekker, A.; Brando, V.; Maughan, M. Dispersal of suspended sediments and nutrients in the Great Barrier Reef lagoon during river-discharge events: Conclusions from satellite remote sensing and concurrent flood-plume sampling. *Mar. Freshw. Res.* **2010**, *61*, 651–664. [CrossRef]
6. Sirjacobs, D.; Alvera-Azcárate, A.; Barth, A.; Lacroix, G.; Park, Y.; Nechad, B.; Ruddick, K.; Beckers, J.-M. Cloud filling of ocean colour and sea surface temperature remote sensing products over the Southern North Sea by the Data Interpolating Empirical Orthogonal Functions methodology. *J. Sea Res.* **2011**, *65*, 114–130. [CrossRef]
7. Ruddick, K.; Neukermans, G.; Vanhellemont, Q.; Jolivet, D. Challenges and opportunities for geostationary ocean colour remote sensing of regional seas: A review of recent results. *Remote Sens. Environ.* **2014**, *146*, 63–76. [CrossRef]
8. Ruddick, K.; Vanhellemont, Q.; Yan, J.; Neukermans, G.; Wei, G.; Shang, S. Variability of suspended particulate matter in the Bohai Sea from the geostationary Ocean Color Imager (GOCI). *Ocean. Sci. J.* **2012**, *47*, 331–345. [CrossRef]
9. IOCCG. *Ocean-Colour Observations from a Geostationary Orbit*; Reports of the International Ocean-Colour Coordinating Group (IOCCG) Report Number 12; Antoine, D., Ed.; IOCCG: Dartmouth, NS, Canada, 2012. Available online: http://ioccg.org/wp-content/uploads/2015/10/ioccg-report-12.pdf (accessed on 18 April 2016).
10. Gruber, R.; Waterhouse, J.; Logan, M.; Petus, C.; Howley, C.; Lewis, S.; Tracey, D.; Langlois, L.; Tonin, H.; Skuza, M.; et al. *Marine Monitoring Program: Annual Report for Inshore water Quality Monitoring 2018–2019*; Report for the Great Barrier Reef Marine Park Authority 2208–4096; Great Barrier Reef Marine Park Authority: Townsville, Australia, 2020. Available online: https://elibrary.gbrmpa.gov.au/jspui/handle/11017/3665 (accessed on 14 May 2022).
11. Waterhouse, J.; Schaffelke, B.; Bartley, R.; Eberhard, R.; Brodie, J.; Thorburn, P.; Rolfe, J.; Ronan, M.; Taylor, B.; Star, M.; et al. *Scientific Consensus Statement Summary: Land Use Impacts on Great Barrier Reef Water Quality and Ecosystem Condition*; State of Queensland: Townsville, Australia, 2017. Available online: https://www.reefplan.qld.gov.au/science-and-research/the-scientific-consensus-statement (accessed on 25 November 2017).
12. Feng, J.; Chen, H.; Zhang, H.; Li, Z.; Yu, Y.; Zhang, Y.; Bilal, M.; Qiu, Z. Turbidity estimation from GOCI satellite data in the turbid estuaries of China's coast. *Remote Sens.* **2020**, *12*, 3770. [CrossRef]
13. Lou, X.; Hu, C. Diurnal changes of a harmful algal bloom in the East China Sea: Observations from GOCI. *Remote Sens. Environ.* **2014**, *140*, 562–572. [CrossRef]
14. Groom, S.; Sathyendranath, S.; Ban, Y.; Bernard, S.; Brewin, R.; Brotas, V.; Brockmann, C.; Chauhan, P.; Choi, J.-K.; Chuprin, A.; et al. Satellite Ocean Colour: Current Status and Future Perspective. *Front. Mar. Sci.* **2019**, *6*, 485. [CrossRef]
15. Park, J.-E.; Park, K.-A.; Kang, C.-K.; Park, Y.-J. Short-Term Response of Chlorophyll-a Concentration to Change in Sea Surface Wind Field over Mesoscale Eddy. *Estuaries Coasts* **2019**, *43*, 646–660. [CrossRef]
16. Lavigne, H.; Ruddick, K. The potential use of geostationary MTG/FCI to retrieve chlorophyll-a concentration at high temporal resolution for the open oceans. *Int. J. Remote Sens.* **2018**, *39*, 2399–2420. [CrossRef]
17. Dorji, P.; Fearns, P. Atmospheric correction of geostationary Himawari-8 satellite data for Total Suspended Sediment mapping: A case study in the Coastal Waters of Western Australia. *ISPRS J. Photogramm. Remote Sens.* **2018**, *144*, 81–93. [CrossRef]
18. Miller, S.D.; Schmit, T.L.; Seaman, C.J.; Lindsey, D.T.; Gunshor, M.M.; Kohrs, R.A.; Sumida, Y.; Hillger, D. A Sight for Sore Eyes: The Return of True Color to Geostationary Satellites. *Bull. Am. Meteorol. Soc.* **2016**, *97*, 1803–1816. [CrossRef]
19. Doxaran, D.; Lamquin, N.; Park, Y.-J.; Mazeran, C.; Ryu, J.-H.; Wang, M.; Poteau, A. Retrieval of the seawater reflectance for suspended solids monitoring in the East China Sea using MODIS, MERIS and GOCI satellite data. *Remote Sens. Environ.* **2014**, *146*, 36–48. [CrossRef]
20. Doxaran, D.; Cherukuru, R.C.N.; Lavender, S.J. Use of reflectance band ratios to estimate suspended and dissolved matter concentrations in estuarine waters. *Int. J. Remote Sens.* **2005**, *26*, 1763–1769. [CrossRef]

21. Kwiatkowska, E.J.; Ruddick, K.; Ramon, D.; Vanhellemont, Q.; Brockmann, C.; Lebreton, C.; Bonekamp, H.G. Ocean colour products from geostationary platforms, opportunities with Meteosat Second and Third Generation. *Ocean. Sci. Discuss.* **2015**, *12*, 3143–3167. [CrossRef]
22. Murakami, H. Ocean color estimation by Himawari-8/AHI. In Proceedings of the Remote Sensing of the Oceans and Inland Waters: Techniques, Applications, and Challenges, New Delhi, India, 7 May 2016. [CrossRef]
23. Chen, X.; Shang, S.; Lee, Z.; Qi, L.; Yan, J.; Li, Y. High-frequency observation of floating algae from AHI on Himawari-8. *Remote Sens. Environ.* **2019**, *227*, 151–161. [CrossRef]
24. Hafeez, S.; Wong, M.S.; Abbas, S.; Jiang, G. Assessing the Potential of Geostationary Himawari-8 for Mapping Surface Total Suspended Solids and Its Diurnal Changes. *Remote Sens.* **2021**, *13*, 336. [CrossRef]
25. Japan Meteorological Agency. *Event Log: Himawari-8 Performance Test Results*; Meteorological Satellite Center: Kiyose, Japan, 2015. Available online: https://www.data.jma.go.jp/mscweb/en/himawari89/space_segment/fig/AHI8_performance_test_en.pdf (accessed on 20 September 2021).
26. IOCCG. *Remote Sensing of Ocean Colour in Coastal and Other Optically-Complex Waters*; Reports of the International Ocean-Colour Coordinating Group (IOCCG) Report Number 3; Sathyendrath, S., Ed.; IOCCG: Dartmouth, NS, Canada, 2000. Available online: http://ioccg.org/wp-content/uploads/2015/10/ioccg-report-03.pdf (accessed on 20 September 2015).
27. Schroeder, T.; Schaale, M.; Lovell, J.; Blondeau-Patissier, D. An ensemble neural network atmospheric correction for Sentinel-3 OLCI over coastal waters providing inherent model uncertainty estimation and sensor noise propagation. *Remote Sens. Environ.* **2022**, *270*, 112848. [CrossRef]
28. Fan, Y.; Li, W.; Chen, N.; Ahn, J.-H.; Park, Y.-J.; Kratzer, S.; Schroeder, T.; Ishizaka, J.; Chang, R.; Stamnes, K. OC-SMART: A machine learning based data analysis platform for satellite ocean color sensors. *Remote Sens. Environ.* **2021**, *253*, 112236. [CrossRef]
29. Brockmann, C.; Doerffer, R.; Peters, M.; Stelzer, K.; Embacher, S.; Ruescas, A. Evolution of the C2RCC neural network for Sentinel 2 and 3 for the retrieval of ocean colour products in normal and extreme optically complex waters. In Proceedings of the European Space Agency, Prague, Czech Republic, 9–13 May 2016.
30. Schroeder, T.; Fischer, J.; Schaale, M.; Fell, F. Artificial-neural-network-based atmospheric correction algorithm: Application to MERIS data. In Proceedings of the SPIE 4892, Ocean Remote Sensing and Applications, Hangzhou, China, 8 May 2003; pp. 124–132. [CrossRef]
31. Jamet, C.; Thira, S.; Moulin, C.; Crepon, M. Use of a Neurovariational Inversion for Retrieving Oceanic and Atmospheric Constituents from Ocean Color Imagery: A Feasibility Study. *J. Atmos. Ocean. Technol.* **2005**, *22*, 460–475. [CrossRef]
32. Brajard, J.; Jamet, C.; Moulin, C.; Thiria, S. Use of a neuro-variational inversion for retrieving oceanic and atmospheric constituents from satellite ocean colour sensor: Application to absorbing aerosols. *Neural Netw. Off. J. Int. Neural Netw. Soc.* **2006**, *19*, 178–185. [CrossRef]
33. Doerffer, R. *Algorithm Theoretical Basis Document (ATBD) MERIS Regional Coastal and Lake Case 2 Water Project Atmospheric Correction ATBD*; Water Version 1; GKSS Research Center: Geesthacht, Germany, 2008; pp. 1–42.
34. Pahlevan, N.; Smith, B.; Schalles, J.; Binding, C.; Cao, Z.; Ma, R.; Alikas, K.; Kangro, K.; Gurlin, D.; Hà, N.; et al. Seamless retrievals of chlorophyll-a from Sentinel-2 (MSI) and Sentinel-3 (OLCI) in inland and coastal waters: A machine-learning approach. *Remote Sens. Environ.* **2020**, *240*, 111604. [CrossRef]
35. Gross, L.; Thiria, S.; Frouin, R.; Mitchell, B.G. Artificial neural networks for modeling the transfer function between marine reflectance and phytoplankton pigment concentration. *J. Geophys. Res. Ocean.* **2000**, *105*, 3483–3495. [CrossRef]
36. Schroeder, T.; Behnert, I.; Schaale, M.; Fischer, J.; Doerffer, R. Atmospheric correction algorithm for MERIS above case-2 waters. *Int. J. Remote Sens.* **2007**, *28*, 1469–1486. [CrossRef]
37. Schroeder, T.; Schaale, M.; Fischer, J. Retrieval of atmospheric and oceanic properties from MERIS measurements: A new Case-2 water processor for BEAM. *Int. J. Remote Sens.* **2007**, *28*, 5627–5632. [CrossRef]
38. Schroeder, T. Fernerkundung von Wasserinhaltsstoffen in Küstengewässern mit MERIS unter Anwendung expliziter und impliziter Atmosphärenkorrekturverfahren (Remote Sensing of Coastal Waters with MERIS on Basis of Explicit and Implicit Atmospheric Correction Algorithms). Ph.D. Thesis, Freie Universität, Berlin, German, 2005. [CrossRef]
39. Patricio-Valerio, L. Exploring Himawari-8 Observations for the Advanced Coastal Monitoring of the Great Barrier Reef. Ph.D. Thesis, James Cook University, Townsville, Australia, 2021. [CrossRef]
40. Fell, F.; Fischer, J. Numerical simulation of the light field in the atmosphere-ocean system using the matrix-operator method. *J. Quant. Spectrosc. Radiat. Transf.* **2001**, *69*, 351–388. [CrossRef]
41. Fischer, J.; Grassl, H. Radiative transfer in an atmosphere–ocean system: An azimuthally dependent matrix-operator approach. *Appl. Opt.* **1984**, *23*, 1032–1039. [CrossRef]
42. Santer, R.; Zagolski, F.; Dilligeard, E. Radiative Transfer Code Comparison for MERIS Vicarious Calibration. In Proceedings of the ENVISAT Validation Workshop, ESRIN, Frascati, Italy, 9–13 December 2002.
43. Committee on Extension to the Standard Atmosphere. *U.S. Standard Atmosphere*; NASA: Washington, DC, USA, 1976.
44. Holben, B.N.; Eck, T.F.; Slutsker, I.; Tanré, D.; Buis, J.P.; Setzer, A.; Vermote, E.; Reagan, J.A.; Kaufman, Y.J.; Nakajima, T.; et al. AERONET—A Federated Instrument Network and Data Archive for Aerosol Characterization. *Remote Sens. Environ.* **1998**, *66*, 1–16. [CrossRef]
45. AERONET. Aerosol Robotic Network. Available online: https://aeronet.gsfc.nasa.gov/cgi-bin/data_display_aod_v3?site=Lucinda&nachal=2&level=3&place_code=10 (accessed on 3 October 2017).

46. Ångström, A. The parameters of atmospheric turbidity. *Tellus* **1964**, *16*, 64–75. [CrossRef]
47. Rothman, L.S.; Barbe, A.; Chris Benner, D.; Brown, L.R.; Camy-Peyret, C.; Carleer, M.R.; Chance, K.; Clerbaux, C.; Dana, V.; Devi, V.M.; et al. The HITRAN molecular spectroscopic database: Edition of 2000 including updates through 2001. *J. Quant. Spectrosc. Radiat. Transf.* **2003**, *82*, 5–44. [CrossRef]
48. Bennartz, R.; Fischer, J. A modified k-distribution approach applied to narrow band water vapour and oxygen absorption estimates in the near infrared. *J. Quant. Spectrosc. Radiat. Transf.* **2000**, *66*, 539–553. [CrossRef]
49. Zhang, T.; Fell, F.; Liu, Z.S.; Preusker, R.; Fischer, J.; He, M.X. Evaluating the performance of artificial neural network techniques for pigment retrieval from ocean color in Case I waters. *J. Geophys. Res. Ocean.* **2003**, *108*, 3286. [CrossRef]
50. Pope, R.M.; Fry, E.S. Absorption spectrum (380–700 nm) of pure water. II. Integrating cavity measurements. *Appl. Opt.* **1997**, *36*, 8710–8723. [CrossRef]
51. Hale, G.M.; Querry, M.R. Optical constants of water in the 200-nm to 200-µm wavelength region. *Appl. Opt.* **1973**, *12*, 555–563. [CrossRef]
52. Bricaud, A.; Morel, A.; Babin, M.; Allali, K.; Claustre, H. Variations of light absorption by suspended particles with chlorophyll-laconcentration in oceanic (case 1) waters: Analysis and implications for bio-optical models. *J. Geophys. Res. Ocean.* **1998**, *103*, 31033–31044. [CrossRef]
53. Babin, M.; Stramski, D.; Ferrari, G.M.; Claustre, H.; Bricaud, A.; Obolensky, G.; Hoepffner, N. Variations in the light absorption coefficients of phytoplankton, nonalgal particles, and dissolved organic matter in coastal waters around Europe. *J. Geophys. Res. Ocean.* **2003**, *108*, 3211. [CrossRef]
54. Morel, A. Optical properties of pure water and pure seawater. In *Optical Aspects of Oceanography*; Nielsen, J.S., Ed.; Academic Press: Cambridge, MA, USA, 1974; pp. 1–24.
55. Babin, M.; Morel, A.; Fournier-Sicre, V.; Fell, F.; Stramski, D. Light scattering properties of marine particles in coastal and open ocean waters as related to the particle mass concentration. *Limnol. Oceanogr.* **2003**, *48*, 843–859. [CrossRef]
56. Zhang, T.; Fell, F.; Fischer, J. Modelling the backscattering ratio of marine particles in Case-2 waters. In Proceedings of the Ocean Optics XVI, Santa Fe, MN, USA, 18–22 November 2002.
57. Minsky, M.; Papert, S.A. *Perceptrons: An Introduction to Computational Geometry*; MIT Press: Cambridge, MA, USA, 1969.
58. Malthouse, E.C. Limitations of nonlinear PCA as performed with generic neural networks. *IEEE Trans. Neural Netw.* **1998**, *9*, 165–173. [CrossRef] [PubMed]
59. Liu, D.C.; Nocedal, J. On the limited memory BFGS method for large scale optimization. *Math. Program.* **1989**, *45*, 503–528. [CrossRef]
60. Japan Meteorological Agency. *Event Log: Update of Calibration Information Used to Correct Himawari-8 AHI Sensitivity Trend*; Meteorological Satellite Center: Kiyose, Japan, 2019. Available online: https://www.data.jma.go.jp/mscweb/en/oper/eventlog/Update_of_Calibration_Information_2019.pdf (accessed on 20 September 2021).
61. Kurucz, R. The solar spectrum: Atlases and line identifications. In Proceedings of the Laboratory and Astronomical High Resolution Spectra, Brussels, Belgium, 29 August–2 September 1995; p. 17.
62. Meteorological Satellite Center. GSICS Himawari-8 Visible and Near-Infrared Vicarious Calibration Guide. Available online: https://www.data.jma.go.jp/mscweb/data/monitoring/gsics/vis/techinfo_visvical.html (accessed on 10 May 2022).
63. Japan Meteorological Agency. *Event Log: Improvement of Himawari-8 Observation Data Quality*; Event log Meteorological Satellite Center: Kiyose, Japan, 2017. Available online: https://www.data.jma.go.jp/mscweb/en/oper/eventlog/Improvement_of_Himawari-8_data_quality.pdf (accessed on 20 September 2021).
64. Qin, Y.; Steven, A.D.L.; Schroeder, T.; McVicar, T.R.; Huang, J.; Cope, M.; Zhou, S. Cloud Cover in the Australian Region: Development and Validation of a Cloud Masking, Classification and Optical Depth Retrieval Algorithm for the Advanced Himawari Imager. *Front. Environ. Sci.* **2019**, *7*, 20. [CrossRef]
65. Great Barrier Reef Marine Park Authority. Great Barrier Reef (GBR) Features (Reef boundaries, QLD Mainland, Islands, Cays, Rocks and Dry Reefs) (GBRMPA) (Version 1.4) [Dataset] 2164DB88-FD79-449E-920F-61C37ADE634B. 1998. Available online: http://www.gbrmpa.gov.au/geoportal/catalog/search/resource/details.page?uuid=%7B41AB3629-B41B-4746-9B75-3822667E5AF3%7D (accessed on 14 May 2022).
66. Emecen, E.; Kara, G.; Erdogmus, F.; Gardashov, R. The determination of sunglint locations on the ocean surface by observation from geostationary satellites. *TAO Terr. Atmos. Ocean. Sci.* **2006**, *17*, 253. [CrossRef]
67. National Oceanic and Atmospheric Administration. Total Ozone Analysis using SBUV/2 and TOVS (TOAST). Available online: https://www.ospo.noaa.gov/Products/atmosphere/toast/index.html (accessed on 1 December 2020).
68. Kistler, R.; Kalnay, E.; Collins, W.; Saha, S.; White, G.; Woollen, J.; Chelliah, M.; Ebisuzaki, W.; Kanamitsu, M.; Kousky, V. The NCEP–NCAR 50-year reanalysis: Monthly means CD-ROM and documentation. *Bull. Am. Meteorol. Soc.* **2001**, *82*, 247–268. [CrossRef]
69. Kanamitsu, M.; Ebisuzaki, W.; Woollen, J.; Yang, S.-K.; Hnilo, J.J.; Fiorino, M.; Potter, G.L. NCEP–DOE AMIP-II Reanalysis (R-2). *Bull. Am. Meteorol. Soc.* **2002**, *83*, 1631–1644. [CrossRef]
70. Kalnay, E.; Kanamitsu, M.; Kistler, R.; Collins, W.; Deaven, D.; Gandin, L.; Iredell, M.; Saha, S.; White, G.; Woollen, J. The NCEP/NCAR 40-year reanalysis project. *Bull. Am. Meteorol. Soc.* **1996**, *77*, 437–472. [CrossRef]
71. National Oceanic and Atmospheric Administration. NCEP Reanalysis 2 Meteorological Data. Available online: https://psl.noaa.gov/data/gridded/data.ncep.reanalysis2.html (accessed on 1 December 2020).

72. Integrated Marine Observing System. IMOS Ocean Colour Bio Optical Database of Australian Waters (SRS-OC-BODBAW). 2011. Available online: https://researchdata.edu.au/imos-srs-ocean-australian-waters (accessed on 20 February 2017).
73. Great Barrier Reef Marine Park Authority. *Marine Monitoring Program Quality Assurance and quality Control Manual 2017–2018*; Great Barrier Reef Marine Park Authority: Townsville, Australia, 2019. Available online: http://elibrary.gbrmpa.gov.au/jspui/handle/11017/3487 (accessed on 15 May 2018).
74. Soja-Woźniak, M.; Baird, M.; Schroeder, T.; Qin, Y.; Clementson, L.; Baker, B.; Boadle, D.; Brando, V.; Steven, A.D.L. Particulate Backscattering Ratio as an Indicator of Changing Particle Composition in Coastal Waters: Observations From Great Barrier Reef Waters. *J. Geophys. Res. Ocean.* **2019**, *124*, 5485–5502. [CrossRef]
75. Bulgarelli, B.; Zibordi, G. On the detectability of adjacency effects in ocean color remote sensing of mid-latitude coastal environments by SeaWiFS, MODIS-A, MERIS, OLCI, OLI and MSI. *Remote Sens. Environ.* **2018**, *209*, 423–438. [CrossRef]
76. Schroeder, T.; Lovell, J.; King, E.; Clementson, L.; Scott, R. *IMOS Ocean Colour Validation Report 2017-18, Report to the Integrated Marine Observing System (IMOS)*; CSIRO Oceans and Atmosphere: Brisbane, Australia, 2018; p. 22.
77. King, E.; Schroeder, T.; Brando, V.; Suber, K. A Pre-operational System for Satellite Monitoring of Great Barrier Reef Marine Water Quality. In *Wealth from Oceans Flagship Report*; CSIRO Wealth from Oceans Flagship: Hobart, Australia, 2014. [CrossRef]
78. Japan Meteorological Agency. *Event Log: Quality Improvement of Himawari-8 Observation Data*; Meteorological Satellite Center: Kiyose, Japan, 2016. Available online: https://www.data.jma.go.jp/mscweb/en/oper/eventlog/20161117_Quality_improvement_of_Himawari-8_observation_data.pdf (accessed on 20 September 2021).
79. Japan Aerospace Exploration Agency. JAXA Himawari Monitor P-Tree System. Available online: https://www.eorc.jaxa.jp/ptree/index.html (accessed on 14 May 2022).
80. Hu, C.; Feng, L.; Lee, Z.; Davis, C.O.; Mannino, A.; McClain, C.R.; Franz, B.A. Dynamic range and sensitivity requirements of satellite ocean color sensors: Learning from the past. *Appl. Opt.* **2012**, *51*, 6045–6062. [CrossRef]
81. Tang, W.; Llort, J.; Weis, J.; Perron, M.M.G.; Basart, S.; Li, Z.; Sathyendranath, S.; Jackson, T.; Sanz Rodriguez, E.; Proemse, B.C.; et al. Widespread phytoplankton blooms triggered by 2019–2020 Australian wildfires. *Nature* **2021**, *597*, 370–375. [CrossRef] [PubMed]
82. Great Barrier Reef Marine Park Authority. *Water Quality Guidelines for the Great Barrier Reef Marine Park*; 1921682299; Great Barrier Reef Marine Park Authority: Townsville, Australia, 2010. Available online: https://elibrary.gbrmpa.gov.au/jspui/handle/11017/432 (accessed on 20 August 2019).
83. Brodie, J.; Grech, A.; Pressey, B.; Day, J.; Dale, A.; Morrison, T.; Wenger, A. The future of the Great Barrier Reef: The water quality imperative. In *Coasts and Estuaries*; Wolanski, E., Day, J.W., Elliott, M., Ramachandran, R., Eds.; Elsevier: Amsterdam, The Netherlands, 2019; pp. 477–499. [CrossRef]
84. Hieronymi, M.; Müller, D.; Doerffer, R. The OLCI Neural Network Swarm (ONNS): A Bio-Geo-Optical Algorithm for Open Ocean and Coastal Waters. *Front. Mar. Sci.* **2017**, *4*, 140. [CrossRef]
85. Donlon, C. *Sentinel-3 Mission Requirements Traceability Document (MRTD)*; European Space Agency (ESA)—ESTEC: Noordwijk, The Netherlands, 2011; p. 234. Available online: https://sentinels.copernicus.eu/documents/247904/1848151/Sentinel-3-Mission-Requirements-Traceability (accessed on 11 October 2018).
86. Doerffer, R. *Protocols for the Validation of MERIS Water Products*; ESA Publication PO-TN-MEL-GS-0043 GKSS; Forschungszentrum: Geesthacht, Germany, 2002; pp. 1–42.
87. Queensland Government. Water Monitoring Information Portal (WMIP). Available online: https://water-monitoring.information.qld.gov.au/ (accessed on 30 March 2021).
88. Wolanski, E.; Spagnol, S. Sticky Waters in the Great Barrier Reef. *Estuar. Coast. Shelf Sci.* **2000**, *50*, 27–32. [CrossRef]
89. Pickard, G.L.; Donguy, J.-R.; Hénin, C.; Rougerie, F. *A Review of the Physical Oceanography of the Great Barrier Reef and Western Coral Sea*; Australian Government Publishing Service: Canberra, Australia, 1977.
90. Feng, D.; Hodges, B.R.; Socolofsky, S.A.; Thyng, K.M. Tidal eddies at a narrow channel inlet in operational oil spill models. *Mar. Pollut. Bull.* **2019**, *140*, 374–387. [CrossRef] [PubMed]
91. De'ath, G.A.; Fabricius, K.K. *Water Quality of the Great Barrier Reef: Distributions, Effects on Reef Biota and Trigger Values for the Protection of Ecosystem Health*; Great Barrier Reef Marine Park Authority Commonwealth of Australia and Australian Institute of Marine Science: Townsville, Australia, 2008; p. 104.
92. Thomson, R.E.; Wolanski, E.J. Tidal period upwelling within Raine island entrance great barrier reef. *J. Mar. Res.* **1984**, *42*, 787–808. [CrossRef]
93. Wolanski, E.; Drew, E.; Abel, K.M.; O'Brien, J. Tidal jets, nutrient upwelling and their influence on the productivity of the alga Halimeda in the Ribbon Reefs, Great Barrier Reef. *Estuar. Coast. Shelf Sci.* **1988**, *26*, 169–201. [CrossRef]
94. Marmorino, G.O.; Smith, G.B.; Miller, W.D. Turbulence characteristics inferred from time-lagged satellite imagery of surface algae in a shallow tidal sea. *Cont. Shelf Res.* **2017**, *148*, 178–184. [CrossRef]
95. Delandmeter, P.; Lambrechts, J.; Marmorino, G.O.; Legat, V.; Wolanski, E.; Remacle, J.-F.; Chen, W.; Deleersnijder, E. Submesoscale tidal eddies in the wake of coral islands and reefs: Satellite data and numerical modelling. *Ocean. Dyn.* **2017**, *67*, 897–913. [CrossRef]
96. Li, G.; He, Y.; Liu, G.; Zhang, Y.; Hu, C.; Perrie, W. Multi-Sensor Observations of Submesoscale Eddies in Coastal Regions. *Remote Sens.* **2020**, *12*, 711. [CrossRef]

97. IOCCG. *Mission Requirements for Future Ocean-Colour Sensors*; Reports of the International Ocean-Colour Coordinating Group (IOCCG) Report Number 13; McClain, C., Meister, G., Eds.; IOCCG: Dartmouth, NS, Canada, 2012. Available online: http://ioccg.org/wp-content/uploads/2015/10/ioccg-report-13.pdf (accessed on 30 September 2017).
98. Neukermans, G.; Ruddick, K.; Bernard, E.; Ramon, D.; Nechad, B.; Deschamps, P.-Y. Mapping total suspended matter from geostationary satellites: A feasibility study with SEVIRI in the Southern North Sea. *Opt. Express* **2009**, *17*, 14029–14052. [CrossRef]
99. Neukermans, G.; Ruddick, K.; Loisel, H.; Roose, P. Optimization and quality control of suspended particulate matter concentration measurement using turbidity measurements. *Limnol. Oceanogr. Methods* **2012**, *10*, 1011–1023. [CrossRef]
100. Röttgers, R.; Heymann, K.; Krasemann, H. Suspended matter concentrations in coastal waters: Methodological improvements to quantify individual measurement uncertainty. *Estuar. Coast. Shelf Sci.* **2014**, *151*, 148–155. [CrossRef]
101. Tilstone, G.; Moore, G.; Sørensen, K.; Doerffer, R.; Røttgers, R.; Ruddick, K.; Pasterkamp, R.; Jørgensen, P. Regional validation of MERIS chlorophyll products in North Sea coastal waters. In Proceedings of the Working meeting on MERIS and AATSR Calibration and Geophysical Validation (ENVISAT MAVT-2003), Frascati, Italy, 20–24 October 2002.
102. Stavn, R.H.; Rick, H.J.; Falster, A.V. Correcting the errors from variable sea salt retention and water of hydration in loss on ignition analysis: Implications for studies of estuarine and coastal waters. *Estuar. Coast. Shelf Sci.* **2009**, *81*, 575–582. [CrossRef]
103. Okuyama, A.; Takahashi, M.; Date, K.; Hosaka, K.; Murata, H.; Tabata, T.; Yoshino, R. Validation of Himawari-8/AHI radiometric calibration based on two years of in-orbit data. *J. Meteorol. Soc. Japan. Ser. II* **2018**, *96*, 91–109. [CrossRef]
104. Japan Meteorological Agency. *Event log: Impacts of Spacecraft Events and Calibration on Himawari-8 Images: Striping*; Meteorological Satellite Center: Kiyose, Japan, 2020. Available online: http://www.data.jma.go.jp/mscweb/en/oper/image_info.html#005 (accessed on 20 September 2021).
105. Moses, W.J.; Bowles, J.H.; Lucke, R.L.; Corson, M.R. Impact of signal-to-noise ratio in a hyperspectral sensor on the accuracy of biophysical parameter estimation in case II waters. *Opt. Express* **2012**, *20*, 4309–4330. [CrossRef]
106. Alvarez-Romero, J.G.; Devlin, M.; Teixeira da Silva, E.; Petus, C.; Ban, N.C.; Pressey, R.L.; Kool, J.; Roberts, J.J.; Cerdeira-Estrada, S.; Wenger, A.S.; et al. A Novel Approach to Model Exposure of Coastal Marine Ecosystems to Riverine Flood Plumes Based on Remote Sensing Techniques. *J. Environ. Manag.* **2013**, *119*, 194–207. [CrossRef]
107. Petus, C.; Devlin, M.; Thompson, A.; McKenzie, L.; Teixeira da Silva, E.; Collier, C.; Tracey, D.; Martin, K. Estimating the Exposure of Coral Reefs and Seagrass Meadows to Land-Sourced Contaminants in River Flood Plumes of the Great Barrier Reef: Validating a Simple Satellite Risk Framework with Environmental Data. *Remote Sens.* **2016**, *8*, 210. [CrossRef]
108. Devlin, M.; Schroeder, T.; McKinna, L.; Brodie, J.; Brando, V.; Dekker, A. Monitoring and Mapping of Flood Plumes in the Great Barrier Reef Based on In Situ and Remote Sensing Observations. In *Advances in Environmental Remote Sensing to Monitor Global Changes*; Chang, N.-B., Ed.; Environmental Remote Sensing and Systems Analysis; CRC Press: Boca Raton, FL, USA, 2012; pp. 147–191. [CrossRef]
109. Steven, A.D.; Baird, M.E.; Brinkman, R.; Car, N.J.; Cox, S.J.; Herzfeld, M.; Hodge, J.; Jones, E.; King, E.; Margvelashvili, N.; et al. eReefs: An operational information system for managing the Great Barrier Reef. *J. Oper. Oceanogr.* **2019**, *12*, S12–S28. [CrossRef]